Monthly Notices of the ROYAL ASTRONOMICAL SOCIETY

MNRAS **535,** 531–550 (2024) https://doi.org/10.1093/mnras/stae2323
Advance Access publication 2024 October 11

K2-370 b: a strongly irradiated sub-Neptune transiting a very active solar-type star

A. Sozzetti [1]★ M. Damasso,[1] J. Fernández Fernández [2,3] A. Mortier [4] A. Anna John,[5] P. E. Cubillos,[1,6] T. G. Wilson [2,5] M. Pinamonti [1] L. Nielsen [7] A. S. Bonomo,[1] A. V. Freckelton [4] A. Collier Cameron [5] D. Armstrong [2,3] A. Vanderburg [8] D. Bayliss [2,3] X. Dumusque,[9] A. Ghedina,[10] M. A. F. Keniger,[2,3] D. W. Latham,[11] M. López Morales,[11] L. Malavolta [12,13] A. Osborn,[14] F. Pepe,[9] R. Rabino,[15] P. A. Strøm,[2] S. Udry[9] and P. Wheatley [2,3]

[1]*INAF – Osservatorio Astrofisico di Torino, Via Osservatorio 20, I-10025 Pino Torinese, Italy*
[2]*Department of Physics, University of Warwick, Gibbet Hill Road, Coventry CV4 7AL, UK*
[3]*Centre for Exoplanets and Habitability, University of Warwick, Gibbet Hill Road, Coventry CV4 7AL, UK*
[4]*School of Physics and Astronomy, University of Birmingham, Edgbaston, Birmingham B15 2TT, UK*
[5]*Centre for Exoplanet Science / SUPA, School of Physics & Astronomy, University of St Andrews, North Haugh ST ANDREWS, Fife KY16 9SS, UK*
[6]*Space Research Institute, Austrian Academy of Sciences, Schmiedlstrasse 6, A-8042 Graz, Austria*
[7]*University Observatory Munich, Ludwig Maximilian University, Scheinerstrasse 1, D-81679 Munich, Germany*
[8]*Department of Physics and Kavli Institute for Astrophysics and Space Researc h, Massac husetts Institute of Technology, Cambridge, MA 02139, USA*
[9]*Astronomy Department of the University of Geneva, Chemin Pegasi 51, CH-1290 Versoix, Switzerland*
[10]*Fundación Galileo Galilei – INAF, Fundación Canaria. Rambla J. A. Fernández Pé rez, 7, E-38712 S. Antonio de B.Baja (S.C. de Tenerife), Spain*
[11]*Center for Astrophysics | Harvard & Smithsonian, 60 Garden Street, Cambridge, MA 02138, USA*
[12]*Dipartimento di Fisica e Astronomia 'Galileo Galilei', Università di Padova, Vicolo dell'Osservatorio 3, I-35122, Padova, Italy*
[13]*INAF – Osservatorio Astronomico di Padova, Vicolo dell'Osservatorio 5, I-35122 Padova, Italy*
[14]*Department of Physics and Astronomy, McMaster University, 1280 Main St W, Hamilton, ON L8S 4L8, Canada*
[15]*Politecnico di Torino, Department of Environment, Land and Infrastructure Engineering (DIATI), Corso Duca degli Abruzzi 24, I-10129 Torino, Italy*

Accepted 2024 September 27. Received 2024 September 26; in original form 2024 May 7

ABSTRACT

We report on the detailed characterization of K2-370 b, a transiting sub-Neptune on a 2.14-d orbit around the chromospherically active G-type dwarf HD 284521 ($T_{\rm eff} = 5662 \pm 44$ K, $< \log R'_{\rm HK} >= -4.49$). The system parameters are derived based on a global fit to K2, *TESS* and CHEOPS photometry, and HARPS-N and HARPS radial velocities (RVs). A Gaussian process regression analysis is performed simultaneously to the orbital fit of the RVs of K2-370 to effectively model the strong stellar rotation signal with a period of 13.5 ± 0.05 d and measure the planetary RV signal with semi-amplitude $K_{\rm b} = 5.6 \pm 0.7\,{\rm m\,s^{-1}}$. We find that K2-370 b has a radius of $2.67 \pm 0.05\,{\rm R_\oplus}$ and a mass of $11.1 \pm 1.4\,{\rm M_\oplus}$. With an estimated equilibrium temperature $T_{\rm eq} \sim 1480$ K, K2-370 b is the second-hottest sub-Neptune with a highly precise mass determination around primaries with $T_{\rm eff} > 5500$ K. The resulting density of $3.2 \pm 0.4\,{\rm g\,cm^{-3}}$ implies that K2-370 b either retains a significant (~ 2 per cent by mass) H-rich atmosphere or its interior contains a high (~ 40 per cent) water–mass fraction.

Key words: methods: miscellaneous – techniques: photometric – techniques: radial velocities – planets and satellites: composition – stars: individual: HD 284521 (K2-370).

1 INTRODUCTION

The sample of small exoplanets that populates the second peak of the bimodal planet–radius distribution (Fulton et al. 2017; Fulton & Petigura 2018; Van Eylen et al. 2018) corresponds to the class of so-called sub-Neptunes. The general consensus is that these planets are unlikely to be entirely rocky in nature, but possess significant mass fractions of volatile compounds (e.g. Lopez, Fortney & Miller 2012; Rogers 2015; Jin & Mordasini 2018; Lozovsky et al. 2018; Bitsch, Raymond & Izidoro 2019; Mousis et al. 2020; Venturini et al. 2020; Bean, Raymond & Owen 2021; Kempton et al. 2023b). The lower bound to the radius of sub-Neptunes should correspond to that of the transition regime between purely rocky super-Earths and volatile-rich planets. This number can be as low as ~ 1.5 (Kempton et al. 2023b) or as high as ~ 2.0 (Bean et al. 2021; Neil, Liston & Rogers 2022), with reference threshold values also identified as being ~ 1.6 (Rogers 2015), ~ 1.7 (Lee, Karalis & Thorngren 2022; Piaulet et al. 2023), ~ 1.75 (Aguichine et al. 2021), and $\sim 1.8\,{\rm R_\oplus}$ (Izidoro et al. 2022), closely matching the relative minimum of the radius gap (Fulton et al. 2017). The upper bound in radius typically corresponds to $\sim 4.0\,{\rm R_\oplus}$, although the value of $\sim 3.5\,{\rm R_\oplus}$ is also used (Fulton et al.

★ E-mail: alessandro.sozzetti@inaf.it

© 2024 The Author(s).
Published by Oxford University Press on behalf of Royal Astronomical Society. This is an Open Access article distributed under the terms of the Creative Commons Attribution License (https://creativecommons.org/licenses/by/4.0/), which permits unrestricted reuse, distribution, and reproduction in any medium, provided the original work is properly cited.

Downloaded from https://academic.oup.com/mnras/article/535/1/531/7819156 by Uni PD user on 04 September 2025

2017; Aguichine et al. 2021), which corresponds to the approximate location where the radius distribution falls to a low and approximately constant value.

The exact boundaries of the sub-Neptune population are somewhat uncertain due to intrinsic degeneracies in the parameter space of mass and radius from theoretical modelling (e.g. Rogers & Seager 2010; Turbet et al. 2020, and references therein). Virtually identical values of these two physical parameters, and therefore inferred bulk densities, can be obtained assuming a solid rock/iron core surrounded by a small hydrogen/helium-dominated gaseous envelope, or a water-rich interior and high-mean molecular weight atmosphere (e.g. Adams, Seager & Elkins-Tanton 2008; Valencia et al. 2013; Lozovsky et al. 2018; Zeng et al. 2019; Aguichine et al. 2021). In the current literature, planets with the former composition go under the name of mini-Neptunes or gas dwarfs, while those with the latter composition are referred to as water worlds. As radii get larger, it is expected that sub-Neptunes (irrespective of their cores being rocky or volatile-rich) should more easily retain envelopes of hydrogen and helium typically amounting to $1-10$ per cent in terms of mass fraction, but also in this case the transition radius is not fully agreed upon, with some studies placing it at $\sim 2.0\,R_\oplus$ (Zeng et al. 2019; Bean et al. 2021), others expecting it at $\sim 2.6\,R_\oplus$ (Lozovsky et al. 2018) or as high as $\sim 3.0\,R_\oplus$ (Otegi, Bouchy & Helled 2020a).

The compositional properties of close-in sub-Neptunes as observed today reflect their formation and evolutionary history. In standard models of low-mass planet formation by core or pebble accretion (e.g. Hansen & Murray 2012; Bodenheimer & Lissauer 2014; Lee & Chiang 2016; Johansen & Lambrechts 2017; Ormel, Vazan & Brouwers 2021) sub-Neptunes form within the snow line and are primarily composed of volatile-poor, rocky material surrounded by a primordial gaseous envelope accreted from the protoplanetary disc. Subsequent atmospheric mass-loss mechanisms, such as photoevaporation (e.g. Owen & Wu 2017; Jin & Mordasini 2018), core-powered mass-loss (e.g. Ginzburg, Schlichting & Sari 2018; Gupta & Schlichting 2019), or giant collisions (Inamdar & Schlichting 2016; MacDonald et al. 2020; Wyatt, Kral & Sinclair 2020) strip most or all the gas from the planets. These scenarios closely reproduce the correct location of the radius gap, and its dependence on other properties such as orbital period and stellar mass (e.g. Berger et al. 2020). Instead, short-period water-rich sub-Neptunes more likely assembled beyond the snow line and then migrated inwards to their present location (e.g. Léger et al. 2004; Luger et al. 2015; Bitsch et al. 2019, 2021; Zeng et al. 2019; Venturini et al. 2020; Izidoro et al. 2021). If the population of such planets is significant, then the bimodality of the radius distribution and the properties of the radius gaps can be interpreted in terms of compositional diversity and not just as signatures of envelope mass-loss mechanisms, particularly if volatile-rich cores of sub-Neptunes are typically more massive than their rocky counterparts (Venturini et al. 2020; Izidoro et al. 2022; Neil et al. 2022). The radius gap might also emerge as a primordial feature, if sub-Neptune formation occurs inside the snow line during the late stages of disc evolution, in gas-poor environments (Lee & Chiang 2016; Lee & Connors 2021; Lee et al. 2022).

Degeneracies in sub-Neptune bulk composition can, in principle, be broken based on observations of the planets' atmospheres, in order to directly determine the presence of H_2/He envelopes or constrain atmospheric abundances of heavier elements, H_2O, in particular (e.g. Miller-Ricci, Seager & Sasselov 2009; Fortney et al. 2013). This would, in turn, allow for deeper insights on the relative role of the different formation pathways in shaping up the properties of the observed population. While earlier atmospheric characterization measurements in the near-infrared with *HST* mostly returned featureless transmission spectra indicative of the ubiquitous presence of high-altitude aerosols and hazes (e.g. Berta et al. 2012; Knutson et al. 2014; Kreidberg et al. 2014; Crossfield & Kreidberg 2017; Guo et al. 2020), the most recent investigations in transmission of a subset of sub-Neptunes has allowed to obtain detections of molecular absorption with variable degree of statistical confidence (e.g. Benneke et al. 2019; Tsiaras et al. 2019; Guilluy et al. 2020; Kreidberg et al. 2020; Madhusudhan et al. 2020; Mikal-Evans et al. 2023; Roy et al. 2023). The growing sample of observed systems has sparked a number of recent studies looking for trends of the degree of cloudiness of small-radius exoplanets' atmospheres with physical parameters, including (but not limited to) planetary temperature, gravity, density, and scale height (e.g. Yu et al. 2021; Dymont et al. 2022; Estrela, Swain & Roudier 2022; Edwards et al. 2023; Brande et al. 2024). The encouraging prospects for detection of strong molecular features in the atmospheres of sub-Neptunes at longer wavelengths with *JWST* (Kawashima & Ikoma 2019) were just recently put to the test with the identification of a metallicity-enhanced atmosphere, with possible presence of water, surrounding GJ 1214 b (based on a *JWST* MIRI mid-infrared phase curve, see Gao et al. 2023; Kempton et al. 2023a) and by the detection of carbon-bearing molecules in the atmosphere of the temperate sub-Neptune K2-18 b (based on *JWST* NIRISS and NIRSpec transmission spectroscopy, see Madhusudhan et al. 2023).

The precise and accurate knowledge of masses and radii, and therefore bulk densities, of sub-Neptunes remain crucial for performing interior structure analyses, for individual objects as well as at the ensemble level (e.g. Lillo-Box et al. 2020; Sozzetti et al. 2021; Luque & Pallé 2022; Castro-González et al. 2023; Rogers, Schlichting & Owen 2023; Cadieux et al. 2024), and to carry out detailed atmospheric characterization (Batalha et al. 2019). As of August 2024, there are 257 sub-Neptunes with $2 \leq R_p \leq 4R_\oplus$[1] and a non-zero mass measurement reported with any precision. This number becomes 196, 127, and 41 with the request of mass measurements good to better than 30, 20, and 10 per cent precision, respectively.[2] The sample of high-precision mass determinations ($\geq 5\sigma$) is biased towards lower mass primaries, with ~ 70 per cent of planets orbiting K and M dwarfs with $T_{\rm eff} \lesssim 5500$ K. This is a simple consequence of the fact that, for similar mass and orbital period, the larger radial–velocity (RV) semi-amplitudes of the planetary signals make high statistical confidence detections easier to attain around later-type stars.

In this paper, we present archival and new K2, *TESS*, and CHEOPS photometry and new RV measurements from the HARPS-N and HARPS high-resolution spectrographs that allow us to obtain a high-precision determination of the orbital and physical parameters of the transiting sub-Neptune K2-370 b, with a period of 2.14 d, discovered by the K2 mission orbiting the $V = 11.1$ mag, chromospherically active G dwarf HD 284 521 (K2-370, TOI-5559), and recently statistically validated by Christiansen et al. (2022). In Section 2, we present the available photometric data and the spectroscopic follow-up observations. Section 3 reports on the determination of the updated properties of the host star, the data analysis and full set of system parameters. Section 4 contains a discussion on the properties of K2-370 b and concluding remarks.

[1]In the remainder of this work, we adopt the radius range for sub-Neptunes from Bean et al. (2021).

[2]Data from the transiting exoplanet catalogue TEPCat (Southworth 2011): https://www.astro.keele.ac.uk/jkt/tepcat/

Downloaded from https://academic.oup.com/mnras/article/535/1/531/7819156 by Uni PD user on 04 September 2025

2 OBSERVATIONS

2.1 K2 photometry

K2-370 was observed by the K2 mission (Howell et al. 2014) during campaign 13 from 2017 March 8 to May 27. The target was monitored in long-cadence mode with integration times of 29.4 min (3605 observations over 79.6 d). The light curve[3] was reduced following the methodology described in Vanderburg & Johnson (2014) and Vanderburg et al. (2016). A total of 37 transits of K2-370 b are present in the light curve, which were first noted by Zink et al. (2021) who had dubbed the candidate EPIC 210797580.01.

2.2 CHEOPS photometry

Two transits of K2-370 b were obtained with CHEOPS (Benz et al. 2021) on 2021 November 9 and 2022 January 2, respectively, under program CH_PR220007 (PI: Mortier. See Table A1 for a log of the observations). The low-altitude Sun-synchronous orbit of CHEOPS results in gaps in the light curve due to the target being occulted by Earth, and passing through the South Atlantic Anomaly. The first visit has an efficiency of 59 per cent, and the second 64 per cent, where efficiency is defined as the percentage of usable scientific data from the observation window. Both observations were conducted with the maximum exposure time of 60s.

Each visit was processed with the CHEOPS Data Reduction Pipeline [DRP, version 14.1.2 (Hoyer et al. 2020)]. The DRP performs calibrations on the raw data based on instrumental information (e.g. dark current, flat field correction, and event flagging) and environmental factors (background flux, cosmic rays, and smearing from nearby objects). Light curves are then extracted for 25 circular apertures, with radii ranging from 15 to 40 pixels. For our analysis, we used the light curves extracted with the R23 apertures for both visits, as these were found to have the highest precision from all extracted light curves. We detrended the light curves using the `PYCHEOPS` package[4] (Maxted et al. 2022). The Point Spread Function (PSF) centroid position (dfdx) and its second differential (d2fdx2) were determined by the package as the optimal decorrelation vectors, hence were used as free parameters in the detrending. An initial least-squares fit was run using these decorrelation vectors, with uniform priors between 0 and 1, and the known K2 parameters of the transit (epoch time, durations, depth, and period) with Gaussian priors based on the preliminary solution reported on the Exoplanet Follow-up Observation Program (ExoFOP) website. A Markov chain Monte Carlo (MCMC) run with 68 walkers and 16 382 steps was implemented via EMCEE (Foreman-Mackey et al. 2013) with a burn-in phase of 1024 steps, using the least-squares fit solution as starting point. Convergence was determined by inspection of the trail plots output by `PyCHEOPS`, as suggested by Maxted et al. (2022). The plotted chains did not display any trend, indicating good convergence was achieved. The trend model returned by the MCMC analysis was removed from the data, leaving us with the flattened light curves for each transit.

2.3 *TESS* photometry

K2-370 (TIC 456945304) was observed with the *TESS* spacecraft (Ricker et al. 2015) in Sector 43 (camera 3, CCD 3) and Sector 44 (camera 2, CCD 4) between 2021 September 16 and November 6, and in Sector 70 (camera 4, CCD 3) and Sector 71 (camera 2, CCD 1) between 2023 September 20 and November 11, totalling 100.76 d of science operations. Individual exposures were combined and processed into 2 min cadence calibrated pixel files and reduced into light curves by the Science Processing Operations Center (SPOC; Jenkins et al. 2016), at NASA Ames Research Center. The Presearch Data Conditioning simple aperture photometric (PDCSAP) light curves (Smith et al. 2012; Stumpe et al. 2012, 2014) were automatically searched for transits using a wavelet-based, noise-compensating matched filter (Jenkins 2002; Jenkins et al. 2010). K2-370 b was detected, passed all diagnostic tests (Twicken et al. 2018; Li et al. 2019), and was subsequently given the name, TOI-5559.01. We retrieved all 2 min PDCSAP data from the Mikulski Archive for Space Telescopes (MAST) portal[5] using the default quality bitmask and rejecting bad quality (`QUALITY` > 0) data points and those with not-a-number fluxes, flux errors, or high background values. This resulted in 61 913 data points from the four *TESS* sectors covering 46 transits of K2-370 b, shown in Fig. 1. Blending from nearby stars in the relatively large *TESS* aperture has been taken into account by the crowding-factor in PDCSAP light curves. Fig. 2 shows the *TESS* aperture with *Gaia* sources down to $\Delta G = 6$ mag over plotted using `tpfplotter` (Aller et al. 2020). The brightest *Gaia* source, with $\Delta G \simeq 2$, in the nearby field is 1 arcmin away, i.e. out of the main SPOC pipeline aperture, and therefore not a cause of worry of possible blend scenarios.

The *TESS* light curve was detrended using the JULIET package (Espinoza, Kossakowski & Brahm 2019) with the CELERITE (Foreman-Mackey et al. 2017) code to fit a transit model constrained by literature values (Vanderburg & Johnson 2014) simultaneously with Gaussian process (GP) regression that adopted a Matern-3/2 kernel. The fitting was performed using the DYNESTY (Speagle 2020) nested sampling algorithm with the Matern-3/2 GP kernel parameterized as follows:

$$k_i(x_l, x_m) = \sigma^2_{\mathrm{GP},i}\left[(1+1/\epsilon)\,\mathrm{e}^{-(1-\epsilon)\sqrt{3}|x_l-x_m|/\rho_{\mathrm{GP},i}}\right] + \\ +\sigma^2_{\mathrm{GP},i}\left[(1-1/\epsilon)\,\mathrm{e}^{-(1+\epsilon)\sqrt{3}|x_l-x_m|/\rho_{\mathrm{GP},i}}\right]. \quad (1)$$

We placed wide log-uniform priors on the amplitude and time-scale hyperparameters (σ_{GP}, ρ_{GP}) of 10^{-6} to 10^3 and 10^{-3} to 10^3, respectively. We set ϵ to 0.01. The flattened *TESS* light curve, along with the CHEOPS and K2 photometric series, was then utilized in the combined analysis described in Section 3.4.

2.4 HARPS-N and HARPS spectroscopy

We collected 76 spectra between 2017 November 29 and 2019 March 23 (480 d) with the HARPS-N high-resolution spectrograph (Cosentino et al. 2012) mounted on the 3.58-m Telescopio Nazionale Galileo in the Canary Islands (Spain). The exposures had a typical exposure time of 1800 sec, and a typical signal-to-noise ratio (SNR)$\sim$ 46. The spectra were reduced and the RVs derived with version 2.3.5 of the HARPS-N Data Reduction Software (DRS) pipeline and a G2-type numerical mask. The HARPS-N RV time-series (reported in Table A2) has a median uncertainty of $\sigma_{\mathrm{RV}} = 2.8\,\mathrm{m\,s^{-1}}$ and rms of $21.7\,\mathrm{m\,s^{-1}}$.

The HARPS spectrograph, mounted at the ESO La Silla (Chile) 3.6-m telescope, was used to gather 60 1800-s exposures of K2-370 between 2022 December 2 and 2023 January 28. The HARPS data

[3]The light curve is freely available at https://lweb.cfa.harvard.edu/~avanderb/k2c13/ep210797580.html

[4]https://github.com/pmaxted/pycheops

[5]https://mast.stsci.edu/portal/Mashup/Clients/Mast/Portal.html

Downloaded from https://academic.oup.com/mnras/article/535/1/531/7819156 by Uni PD user on 04 September 2025

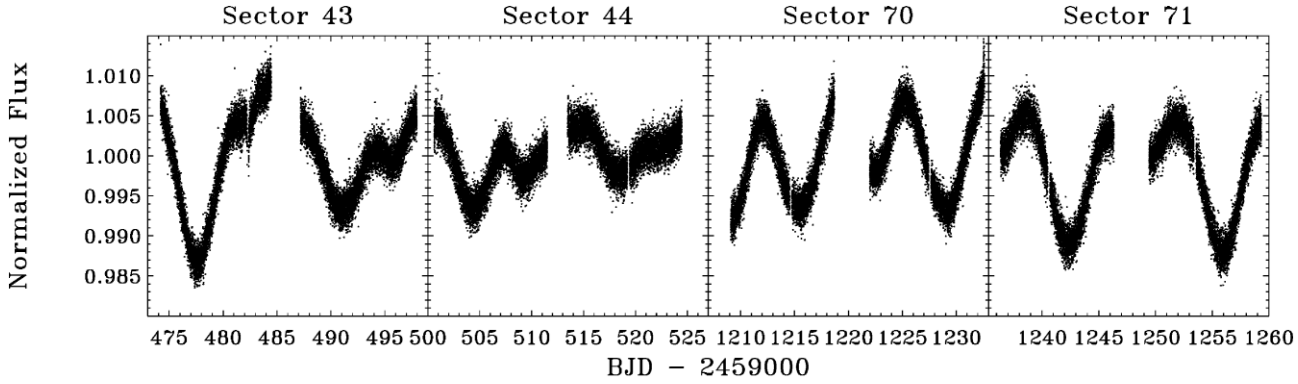

Figure 1. *TESS* light curve of K2-370 from Sectors 43, 44, 70, and 71. The gaps occurring in between and at the mid-point of adjacent sectors are due to telemetry operations around spacecraft periastron passage.

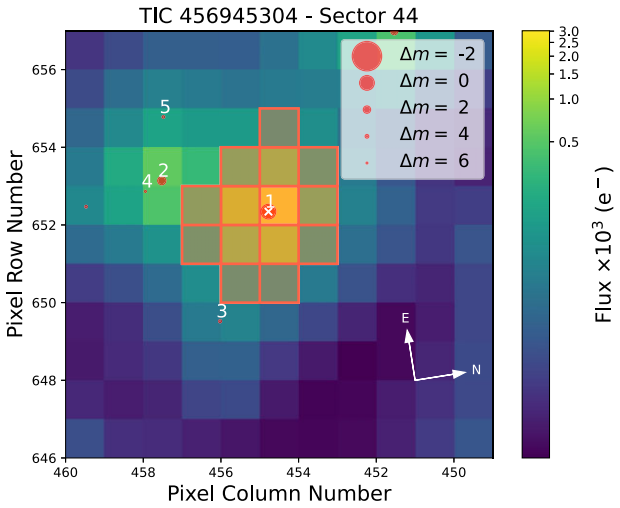

Figure 2. *TESS* aperture for K2-370 in Sector 44 showing nearby *Gaia* sources brighter than $\Delta G = 6$ mag. The red-shaded region identifies the SPOC pipeline aperture. Sources from the *Gaia* DR3 catalogue are overlaid with symbol sizes proportional to the magnitude difference with the target, which is identified with a white cross.

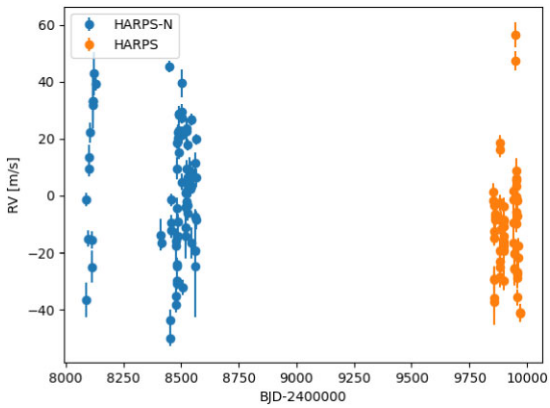

Figure 3. Time series of the HARPS-N (blue-filled circles) and HARPS (orange filled circles) RVs for K2-370.

have a typical SNR∼ 35. The reduction of the HARPS spectra and RV derivation was performed with the same DRS version (and same mask) used for the HARPS-N data. The HARPS RV time series (reported in Table A3) has a median uncertainty of $\sigma_{\rm RV} = 3.2\,{\rm m\,s^{-1}}$ and rms of $17.9\,{\rm m\,s^{-1}}$.

We also report in Tables A2 and A3 the HARPS-N and HARPS time-series of the three spectroscopic activity indicators full width at half-maximum (FHWM), bisector inverse slope (BIS), and chromospheric S-index. The full width at half-maximum (FWHM) and BIS are calculated from the spectral cross-correlation function (CCF), while the S-index is the standard Mount Wilson chromospheric index calculated by the DRS from the calcium (Ca) H&K lines.

Based on standard mass–radius relations (e.g. Chen & Kipping 2017), Christiansen et al. (2022) reported an expected RV semi-amplitude $K \simeq 5\,{\rm m\,s^{-1}}$ for K2-370 b. The RV scatter in both the HARPS and HARPS-N data sets (as shown in Fig. 3) clearly indicates that the planetary signal is dominated by other sources of RV variability.

3 DATA ANALYSIS

3.1 Host star properties

K2-370 is a G5 dwarf star located 140 pc away (Bailer-Jones et al. 2021). The available parameters for this object, from the literature or derived in this work, are listed in Table 1.

We used the HARPS-N spectra to derive the atmospheric stellar parameters; effective temperature, surface gravity, metallicity, microturbulence, and projected rotational velocity. The first three parameters were derived via two methods and we adopt their inverse-variance weighted average as our final parameters.

In a first method, we employed the spectral synthesis code SPC (spectral parameter classification – Buchhave et al. 2012, 2014). Each HARPS-N spectrum was analysed individually after which the results were averaged, weighted by the SNR of each spectrum. During the analysis, the value of surface gravity was additionally constrained through the use of the YY isochrones (Yi et al. 2001). We found $T_{\rm eff} = 5637 \pm 50$ K, $\log g = 4.50 \pm 0.10$ dex, and [m/H]= 0.07 ± 0.08 dex. We note that the global metallicity [m/H] derived through SPC is comparable to the iron abundance [Fe/H] due to the overwhelming presence of iron lines in the optical spectrum. SPC furthermore allowed us to determine the projected rotational velocity, $v \sin i_\star = 3.3 \pm 0.5\,{\rm km\,s^{-1}}$.

The second method used the ARES + MOOG codes and is detailed in Sousa (2014). It used the co-added HARPS-N spectrum and assumed local thermodynamic equilibrium and Kurucz Atlas

Downloaded from https://academic.oup.com/mnras/article/535/1/531/7819156 by Uni PD user on 04 September 2025

Table 1. Astrometry, photometry, and spectroscopically derived stellar properties of HD 284521.

HD 284521, TIC 456945304, TYC 1273-922-1, K2-370		
Parameter	Value	References
Astrometry		
α (J2000)	04:31:16.96	[1, 2, 3]
δ (J2000)	+19:49:54.50	[1, 2, 3]
μ_α (mas yr^{-1})	-33.760 ± 0.022	[1, 2, 3]
μ_δ (mas yr^{-1})	-27.108 ± 0.014	[1, 2, 3]
ϖ (mas)	7.09 ± 0.02	[1, 2, 3]
d (pc)	$140.18^{+0.37}_{-0.45}$	[4]
Photometry		
B_T (mag)	11.72 ± 0.11	[5]
V_T (mag)	11.11 ± 0.10	[5]
G (mag)	10.886 ± 0.003	[1, 6]
J (mag)	9.667 ± 0.027	[7]
H (mag)	9.247 ± 0.059	[7]
K_s (mag)	9.237 ± 0.022	[7]
$W1$ (mag)	9.172 ± 0.023	[8]
$W2$ (mag)	9.219 ± 0.020	[8]
$W3$ (mag)	9.069 ± 0.053	[8]
Stellar parameters		
$T_{\rm eff}$ (K)	5662 ± 44	[9]
log g (dex)	4.48 ± 0.08	[9]
[Fe/H] (dex)	0.08 ± 0.05	[9]
[Mg/H] (dex)	0.12 ± 0.09	[9]
[Si/H] (dex)	0.09 ± 0.05	[9]
ξ (km s^{-1})	1.21 ± 0.06	[9]
$M_\star$ ($M_\odot$)	$0.962^{+0.035}_{-0.038}$	[9]
$R_\star$ ($R_\odot$)	$0.945^{+0.008}_{-0.008}$	[9]
$\varrho_\star$ ($\varrho_\odot$)	$1.14^{+0.06}_{-0.06}$	[9]
$v \sin i_\star$ (km s^{-1})	3.3 ± 0.5	[9]
$P_{\star,\rm rot}$ (d)	13.55 ± 0.08	[9]
$< \log R'_{HK} >$	-4.49 ± 0.03	[9]
$t_{\rm iso}$ (Gyr)	$4.9^{+2.3}_{-2.1}$	[9]
$t_{\rm gyro}$ (Gyr)	1.4 ± 0.4	[9]

References – [1] Gaia Collaboration et al. (2021); [2] Gaia Collaboration et al. (2023); [3] Lindegren et al. (2021); [4] Bailer-Jones et al. (2021); [5] Høg et al. (2000); [6] Evans et al. (2018); [7] Cutri et al. (2003); [8] Cutri et al. (2014); and [9] this work.

9 plane–parallel model atmospheres (Kurucz 1993). The surface gravity was corrected for accuracy following Mortier et al. (2014) and we added systematic errors in quadrature following Sousa et al. (2011). We found $T_{\rm eff} = 5686 \pm 72$ K, log $g = 4.47 \pm 0.12$ dex, and [Fe/H]$= 0.09 \pm 0.05$ dex. This method additionally allowed the derivation of the microturbulence velocity ξ. Using ARES + MOOG, we also measured the individual chemical abundances of magnesium [Mg/H] and silicon [Si/H] (Mortier et al. 2013).

Using the spectroscopic parameters, we could then refine the values of stellar mass, radius and age. To do this, we performed an analysis based on isochrones and evolutionary tracks, using both the Dartmouth and MIST stellar models (Dotter et al. 2008; Dotter 2016). As input, we used the spectroscopically determined effective temperature and metallicity, broad-band photometry in eight bands (all those listed in Table 1 except for the *GaiaG*-band value), and the *Gaia* DR3 parallax (Lindegren et al. 2021; Gaia Collaboration et al. 2023). We ran the analysis four times, allowing for the use of the individual spectroscopic results and the different stellar models. Our final adopted parameters and errors represent the median and 16th, 84th percentile of the combined posterior distributions. More details can be found in Mortier et al. (2020).

The relatively loose age constraint points towards a star with a similar age to the Sun. However, following, for example, Lovis et al. (2011), by converting the Mount Wilson S-index into the $R'_{\rm HK}$ index, which measures chromospheric emission in the cores of the broad photospheric Ca II H&K absorption lines normalized to the underlying photospheric spectrum, we derive an average log $R'_{\rm HK} = -4.49$. The activity levels are more typical of a star younger than the Sun. Standard age–rotation–activity relations (e.g. Noyes et al. 1984; Donahue 1998; Mamajek & Hillenbrand 2008) point to a rotation period $P_{\rm rot}$ shorter than 10 d and $t < 1$ Gyr. As we show in the following sections, we estimate $P_{\rm rot} \simeq 13.5$ d, which is significantly shorter than the range ($P_{\rm rot} \sim 18-40$ d) expected for a star with $t = 4.9 \pm 2.2$ Gyr, based on the rotational evolution models by Johnstone, Bartel & Güdel (2021). Given the measured rotation period, the inference from gyrochronology is that the age of K2-370 is more likely in the range 1.3−1.5 Gyr (e.g. Brown 2014, and references therein), in line with the expectations from the Johnstone et al. (2021) models. We report both age estimates for K2-370 in Table 1, as this can have an impact on the system's evolutionary history (see Section 4.2). We note that discrepancies between age estimates from gyrochronology and isochrone fitting for exoplanet host stars have been discussed in the past (e.g. Saffe, Gómez & Chavero 2005; Brown 2014; Maxted, Serenelli & Southworth 2015), with no clear conclusions.

3.2 Photometry-only analysis

The top panel of Fig. 4 shows the K2 light curve (with the transits of K2-370 b masked). To estimate the stellar rotation period and assess the star spots' decay times, we followed the procedure described in section 3.1 of López-Morales et al. (2016). We calculated the autocorrelation function (ACF) for unevenly sampled time series using the method developed by Edelson & Krolik (1988), implemented in the PYTHON code PYDCF.[6] The ACF peaks occur at time lags which corresponds to integer multiple of the rotation period of the star (major peaks), or its first harmonic (secondary peaks). The decay time of the spots can be estimated by determining the decay time-scale of the amplitude of the ACF main peaks. To measure the rotation period and spots' decay time-scale, we fitted the ACF with a model function for an underdamped simple harmonic oscillator (uSHO)

$$\mathrm{ACF} = \mathrm{e}^{-At}[B\cos(\omega t) + C\cos(2\omega t) + D\cos(3\omega t)] + \gamma_{\rm ACF}. \quad (2)$$

where A is the spot decay time-scale of the ACF (in d^{-1}), ω is equal to $2\pi/P_{\star,\rm rot}$ (in d^{-1}), B, C, and D are coefficients representing the amplitudes of the cosine terms, and $\gamma_{\rm ACF}$ is an offset. We fitted the uSHO model to the ACF using the Monte Carlo (MC) nested sampler and Bayesian inference tool `MULTINEST V3.10` (e.g. Feroz et al. 2019), through the `pyMULTINEST` wrapper (Buchner et al. 2014), with uniform priors on all the model parameters. We find $P_{\star,\rm rot} = 13.4509 \pm 0.0006$ d, and $A = 0.003\,36 \pm 0.000\,06$ d^{-1}. The best-fitting model of equation (2) is shown in Fig. 4 (bottom panel).

The four sectors from *TESS* cover a similar number of stellar rotations to those observed in the K2 light curve. The stellar rotation is clearly detected in *TESS* as well, in both SPOC-PDCSAP and SPOC-SAP data products. Using a generalized Lomb–Scargle periodogram approach (GLS; Lomb 1976; Scargle 1982; Zechmeister & Kürster 2009) on the K2 and *TESS* data while masking out the planetary transits, we find consistent stellar rotation periods of 13.5 ± 0.8 d in 2017 (K2) and 13.2 ± 1.1 d in 2021 and 2023 (*TESS*). The GLS

[6] https://github.com/astronomerdamo/pydcf

Downloaded from https://academic.oup.com/mnras/article/535/1/531/7819156 by Uni PD user on 04 September 2025

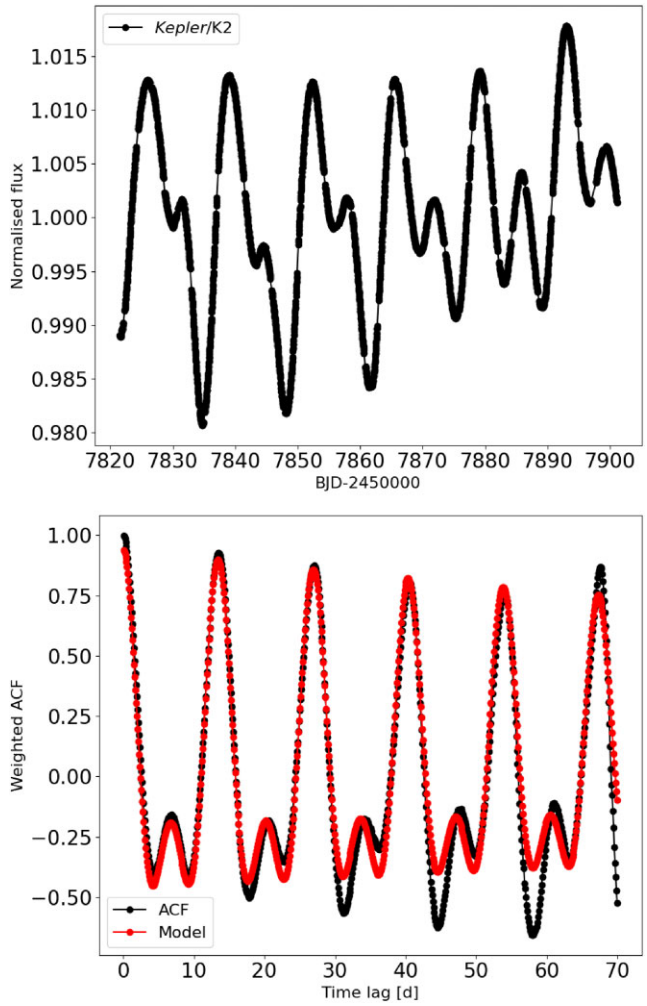

Figure 4. Top panel: *Kepler*/K2 light curve of K2-370. Transits of K2-370 *b* have been masked. Bottom panel: ACF of the K2 light curve, and the corresponding best-fitting model (red dots) for an uSHO.

periodograms of the two data sets are shown in Fig. 5. We use an adapted approach of the GLS, that includes the first two terms of the Fourier series instead of the default single-term periodogram (see e.g. Colman et al. 2024). This ensures more robust signal detection in time-series that contain multiple frequencies and, as in the case of K2-370 that presents two 'wiggles' per rotation, signals with higher harmonic complexity. The peak-to-peak variation of ∼3 per cent has not changed significantly between the two missions, though there are amplitude variations on shorter time-scales, for example, captured in the K2 time series spanning 80 d as shown in Fig. 4. The unchanged activity signature could indicate that the spot configuration on the stellar surface is stable over several years, that stellar spots tend to form at the same latitudes and/or that the star has little differential rotation. Finally, we note that, given the $R_\star$ and $v \sin i\star$ values from Table 1, we can place a 1σ upper limit on the stellar rotation period of $P_{\star,\rm rot} < 16.5$ d, which indicates that $\sin i_\star$ might not be far from unity.

3.3 Spectroscopic analysis of stellar activity

We performed a frequency content analysis of the RVs and spectroscopic activity diagnostics derived from the HARPS-N and HARPS

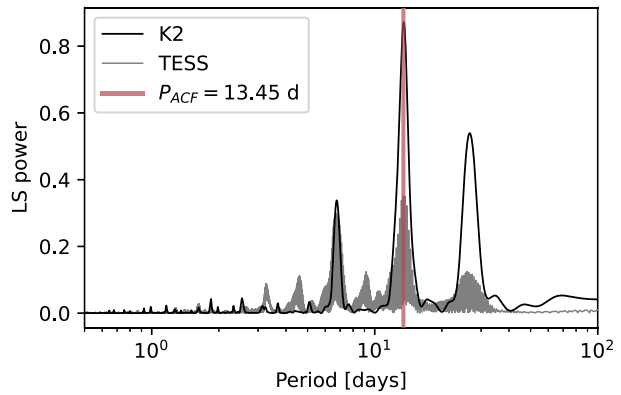

Figure 5. GLS periodograms of the K2 and *TESS* light curves. The periodograms were computed using two terms of the Fourier series to account for the harmonic complexity of the light curves showing two 'wiggles' per stellar rotation. The stellar rotation period of 13.5 d is found to be consistent between the two data sets and the period found with the ACF approach.

spectra to investigate which are the dominant signals in the data sets of the two individual instruments. We analysed the RVs, FHWM, BIS, *S*-index. The GLS periodograms of each data set are shown in Figs 6 and 7. The levels of false alarm probability (FAP) were calculated using a bootstrap (with resampling) analysis of 10 000 simulated time series. The RV time series are dominated by statistically significant signals at the same stellar rotation period identified in the photometry (or its harmonics), which show their counterpart in the periodogram of the activity diagnostics. This result implies that it is necessary to include a term in the model of the RVs that describes the observed variability due to stellar activity. The structure of the periodograms is different for HARPS-N and HARPS, suggesting that the properties of the stellar activity signal, as seen in the spectroscopic data, have changed over the time interval of nearly 3.5 yr between the HARPS-N and HARPS observations. This result indicates that it is appropriate to model the activity term in the RVs by differentiating between HARPS-N and HARPS.

3.4 Combined modelling and system parameters

We derived the orbital and fundamental physical parameters of K2-370 *b* through a joint fit of RVs and transit photometry. We used the detrended transit light curves collected by K2, *TESS*, and CHEOPS. We explored the full parameter space within the imposed priors using `MultiNest v3.10`. The MC setup included 500 live points, a sampling efficiency of 0.3, and a Bayesian evidence tolerance of 0.5. We used the code `batman` (Kreidberg 2015) for modelling the photometric transits. The full RV model includes a Keplerian to fit the planetary Doppler signal (a circular orbit with eccentricity $e_{\rm b} = 0$ was also used), an offset γ for each spectrograph, and a secular acceleration $\dot{\gamma}$. The signal due to the stellar activity has been modelled using a GP regression, adopting the quasi-periodic (QP) kernel. An element of the QP covariance matrix (e.g. Haywood et al. 2014) is defined as follows:

$$k_{QP}(t,t') = h^2 \cdot \exp\left[-\frac{(t-t')^2}{2\lambda^2} - \frac{\sin^2\left(\pi(t-t')/\theta\right)}{2w^2}\right] + \\ + \left(\sigma^2_{\rm RV}(t) + \sigma^2_{\rm jit}\right) \cdot \delta_{t,t'}. \quad (3)$$

Downloaded from https://academic.oup.com/mnras/article/535/1/531/7819156 by Uni PD user on 04 September 2025

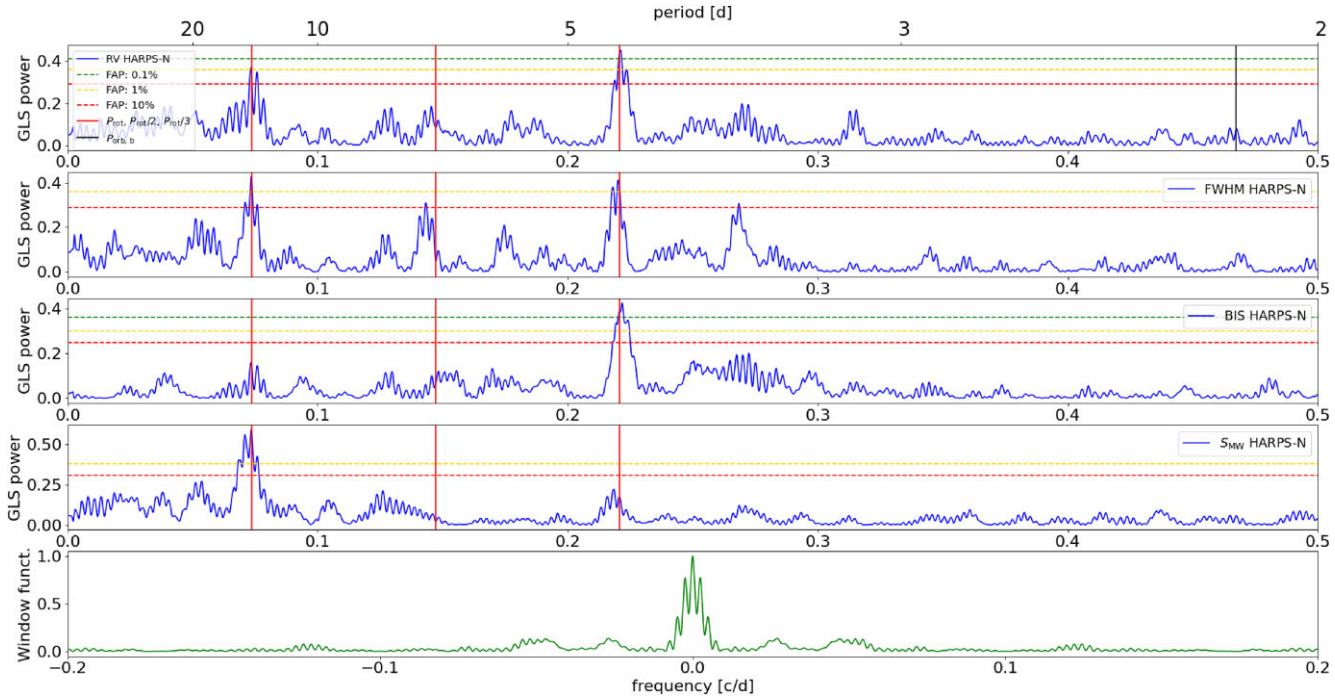

Figure 6. GLS periodograms of RVs and activity diagnostics for HARPS-N data. The horizontal dashed lines of different colours correspond to different levels of FAP. The three vertical solid red lines indicate the location of $P_{\rm rot}$, $P_{\rm rot}/2$, and $P_{\rm rot}/3$, and the vertical black solid line marks the orbital period of K2-370 b.

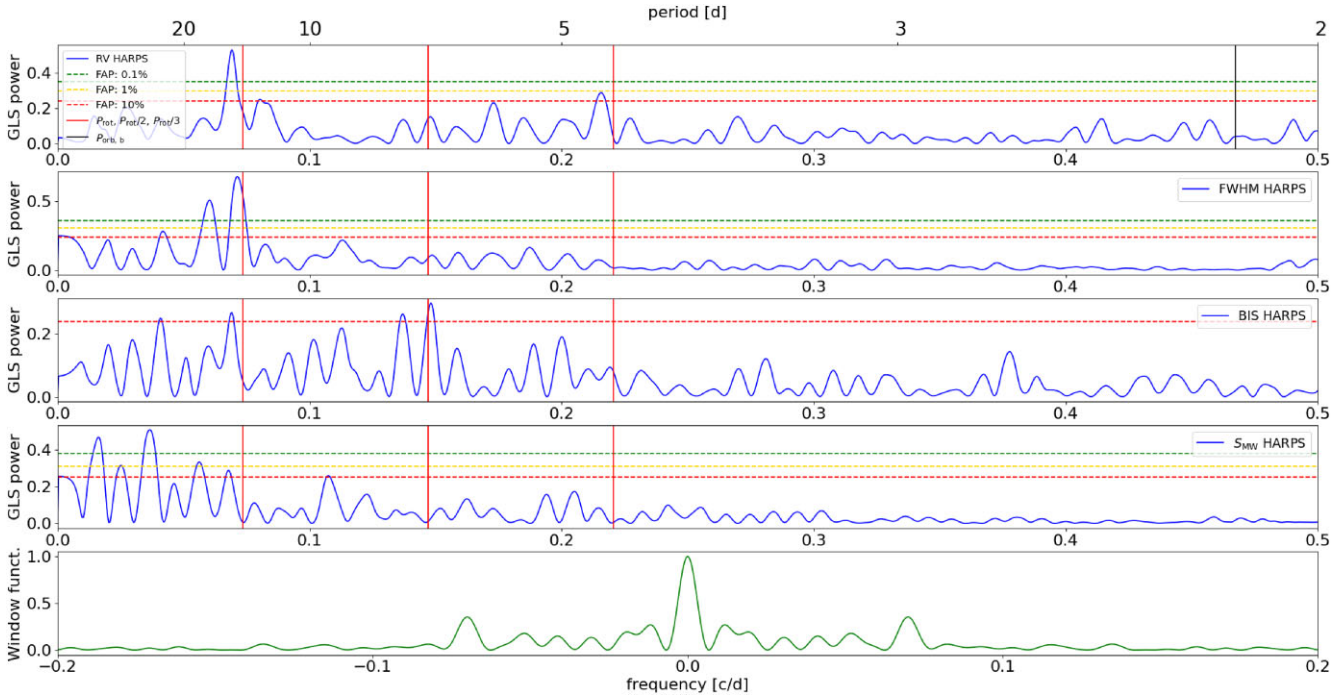

Figure 7. Same as Fig. 6 but for HARPS data.

Here, t and t' represent two different epochs of observations, $\sigma_{\rm RV}$ is the RV uncertainty, and $\delta_{t,t'}$ is the Kronecker delta. Our analysis takes into account other sources of uncorrelated noise – instrumental and/or astrophysical – by including a constant jitter term $\sigma_{\rm jit}$ for each spectrograph, which is added in quadrature to the formal uncertainties $\sigma_{\rm RV}$. The GP hyperparameters are h, which denotes the scale amplitude of the correlated signal; θ, which represents the periodic time-scale of the correlated signal, and corresponds to the stellar rotation period; w, which describes the 'weight' of the rotation period harmonic content within a complete stellar rotation[7] (i.e. a low value of w indicates that the periodic variations contain a significant

[7]The w parameter is often referred to as harmonic complexity.

Downloaded from https://academic.oup.com/mnras/article/535/1/531/7819156 by Uni PD user on 04 September 2025

contribution from the harmonics of the rotation periods); and λ, that represents the decay time-scale of the correlations, and is related to the temporal evolution of the magnetically active regions responsible for the correlated signal observed in the RVs. As discussed in Section 3.3, HARPS-N and HARPS RVs show a different temporal pattern of the activity signal, thus we used a set of hyperparameters h, w, and λ for each spectrograph, while using a single rotation period θ. We used the publicly available PYTHON module GEORGE v0.2.1 (Ambikasaran et al. 2015), integrated within the MultiNest framework, to perform the GP regression.

Concerning the modelling of the light curve, in place of $a_b/R_\star$, we used the stellar density ρ_* as a free parameter (e.g. Sozzetti et al. 2007) with a Gaussian prior based on the mass and radius derived in Section 3.1, from which we derived the $a_b/R_\star$ ratios at each step of the MC sampling. We adopted a quadratic law for the limb darkening, and fitted the coefficients u_1 and u_2 (two sets, one in common for K2 and CHEOPS, one for *TESS*) using the parametrization and uniform priors for coefficients q_1 and q_2 given by Kipping (2010, see equations 15 and 16 therein). We used only one planet-to-star radius ratio $R_b/R_\star$ as a free parameter to fit the transits observed by all the telescopes. We also introduced constant jitters σ_{jit} added in quadrature to the nominal photometric uncertainties, one jitter term for each telescope. Since the *Kepler*/K2 light curve has a cadence of 29.4 min, in order to mitigate morphological distortions introduced when fitting transit light curves with such a long cadence (see e.g. Kipping 2010), we used an oversampling factor of 15. This means that each simulated photometric data point at the epoch of a real observation is calculated as the average value of fifteen evenly spaced simulated data points each corresponding nearly to a 2 min exposure.

For the model where the eccentricity e_b and the argument of periastron $\omega_{\star,b}$ are treated as free parameters, we used the alternative parameterization $\sqrt{e_b}\cos\omega_{\star,b}$ and $\sqrt{e_b}\sin\omega_{\star,b}$ instead of fitting e_b and $\omega_{\star,b}$ directly. The list of priors and their values is provided in the first two columns of Table 2.

Interestingly, in the solution with the eccentricity as a free parameter, we obtain a configuration with a more central transit, lower HARPS-N jitter, and most importantly $e_b = 0.31^{+0.04}_{-0.06}$, formally $> 6\sigma$ significant. However, by comparing the values of the Bayesian evidence $\ln \mathcal{Z}$ calculated by `MultiNest`, we find that the model with the eccentricity treated as a free parameter is not strongly favoured over the circular approximation ($\Delta \ln \mathcal{Z} = +2.5$, which only denotes weak to moderate statistical significance). At the orbital separation of K2-370 b, adopting standard prescriptions for the tidal quality factors of the star ($Q'_s = 10^6$) and planet ($Q'_p = 10^4$), the tidal circularization time-scale for an initial eccentricity of 0.3 would be 9.9 Myr (e.g. Matsumura, Takeda & Rasio 2008; Matsumura, Peale & Rasio 2010), much shorter than t_{gyro}. Therefore, we adopt the circular approximation $e_b = 0$ as the preferred description of the K2-370 b orbit. The three panels of Fig. 8 show the phase-folded best-fitting orbital solution and snapshots of the GP model applied to sections of the HARPS-N and HARPS RVs. The three panels of Fig. 9 show instead the phase-folded best-fitting transit model superposed to the K2, *TESS*, and CHEOPS photometry. The results for all model parameters in both the Keplerian and circular orbit cases are given in the last two columns of Table 2.

3.5 Independent analysis using TWEAKS

Using the TWEAKS pipeline, the HARPS + HARPS-N CCFs were independently examined for planetary signals. By integrating the wavelength-domain and time-domain stellar activity mitigation, TWEAKS was explicitly created to achieve a sub-m s^{-1} detection threshold at extended orbital periods (Anna John, Collier Cameron & Wilson 2022; Anna John et al. 2023). In TWEAKS, the wavelength domain part of the pipeline disentangles the apparent RV variations caused by spectral line-shape changes (stellar activity component) from the Doppler shifts (planet component) (Collier Cameron et al. 2021), while the time-domain counterpart performs a rigorous search for the Doppler shifts in the isolated shift-RVs using a trans-dimensional nested sampler (Faria et al. 2018). The main motivation for using TWEAKS is to (1) cross-verify the mass of the transiting planet, (2) decorrelate against stellar activity-driven CCF shape variations, and (3) using the nested sampler to marginalize potential additional Keplerian signals below the detection threshold, which would also contribute correlated noise.

We obtained a set of basis vectors, which are the major contributors to the spectral-line shape, by performing principal-component analysis of the CCF's ACF using SCALPELS (Collier Cameron et al. 2021). Subsequently, these vectors were incorporated in KIMA (Faria et al. 2018) for stellar-activity decorrelation, following Anna John et al. (2022)

To guard against the possibility of some shift-like activity signals leaking through the SCALPELS signal separation, any remaining rotationally modulated signals were modelled with GP regression applied to the RVs. We adopted the same QP GP kernel representation of equation (3.4), using log-uniform priors on the active-region evolution time-scale of $10 < \lambda < 60$ d and amplitude of $-0.7 < \ln(h) < 20$. The priors on the stellar rotation period were set to be uniform with $10 < \theta < 20$ d, based on estimates from the photometry and a few preliminary runs with uninformative priors. In order to constrain the log harmonic complexity, a uniform prior $-1 < \ln(\sqrt{2}w) < 0$ was adopted. A white noise term σ_{jit}, with a uniform prior $0.5 < \ln(\sigma_{jit}) < 107.414$, is also included in the GP regression. It is implemented in exactly the same manner as mentioned in equation (3.4). The upper limit on this jitter term is defined by the total span of observations. In brief, we employed a QP GP regression combined with a model that included up to three unknown Keplerian signals (in addition to the 'known' transiting planet for which we used the *TESS* transit ephemeris to model the Keplerian), while simultaneously performing stellar activity decorrelation against the SCALPELS basis vectors. For the 'known' planet, we used Gaussian priors to constrain the period, semi-amplitude and mid-transit time based on the *TESS* transit observations.

Subsequently, we obtained a 7.5σ detection of planet b and found that models with additional Keplerian signals are disfavoured, based on the ratios of Bayes factors. In other words, when comparing the Bayes factors of models with zero, one, two, or three additional non-transiting planets, zero was preferred. However, marginalizing over the potential existence of unidentified companion planets permitted their impact to be considered during the posterior sampling process for the reflex RV semi-amplitude of planet b. We then reduced the number of unknown Keplerians down to zero. The joint posteriors now detected a Keplerian signal at orbital period 2.1409 ± 0.0001 d, corresponding to planet b, while constraining stellar rotation to $P_{\star,rot} = 13.58 \pm 0.09$ d. The period determination uncertainty is considerably higher due to the fact that TWEAKS operates with RVs alone and does not use a tight prior from transit photometry, unlike the other methods used in this study. The signal has an RV semi-amplitude of 6.41 ± 0.83 m s^{-1}, which translates into a planetary mass of $12.6 \pm 1.6\,M_\oplus$, when combining with the stellar mass of $0.962\,M_\odot$ and orbital inclination of 84.4° based on Tables 1 and 2, respectively. All the relevant numbers are therefore compatible with

Downloaded from https://academic.oup.com/mnras/article/535/1/531/7819156 by Uni PD user on 04 September 2025

Table 2. Best-fitting values of the one-planet models applied to RVs and transit photometry.

Parameter	Prior	Best-fitting value[a]	
		$e_b = 0$	Free e_b
Fitted (hyper)parameters			
GP hyperparameters			
$h_{HARPS-N}$ ($m\,s^{-1}$)	$\mathcal{U}(0,100)$	$24.54^{+5.25}_{-3.72}$	$24.86^{+5.66}_{-3.86}$
h_{HARPS} ($m\,s^{-1}$)	$\mathcal{U}(0, 100)$	$37.71^{+16.93}_{-10.31}$	$37.93^{+18.19}_{-10.55}$
$\lambda_{HARPS-N}$ (d)	$\mathcal{U}(0, 1000)$	$37.07^{+7.02}_{-5.01}$	$36.00^{+5.33}_{-4.59}$
λ_{HARPS}(d)	$\mathcal{U}(0, 1000)$	$42.47^{+10.07}_{-8.34}$	$43.67^{+10.58}_{-8.66}$
$w_{HARPS-N}$	$\mathcal{U}(0, 1)$	$0.33^{+0.05}_{-0.04}$	$0.33^{+0.05}_{-0.04}$
w_{HARPS}	$\mathcal{U}(0, 1)$	$0.50^{+0.12}_{-0.10}$	$0.48^{+0.13}_{-0.10}$
θ (d)	$\mathcal{U}(0, 15)$	13.55 ± 0.08	13.56 ± 0.08
Planet-related parameters			
K_b ($m\,s^{-1}$)	$\mathcal{U}(0, 20)$	5.6 ± 0.7	5.9 ± 0.7
orbital period, P_b (d)	$\mathcal{U}(2.13, 2.15)$	$2.1408\,093 \pm 0.000\,0012$	$2.1408\,091 \pm 0.000\,0012$
$T_{conj,\,b}$ (BJD-2450000)	$\mathcal{U}(7860.6, 7860.75)$	7860.71859 ± 0.00042	$7860.718\,62 \pm 0.000\,42$
$\sqrt{e_b}\cos\omega_{\star,\,b}$	$\mathcal{U}(-1, 1)$	–	0.04 ± 0.12
$\sqrt{e_b}\sin\omega_{\star,\,b}$	$\mathcal{U}(-1, 1)$	–	$0.544^{+0.034}_{-0.065}$
$R_b/R_\star$	$\mathcal{U}(0.0, 0.1)$	$0.025\,94 \pm 0.000\,41$	$0.024\,43 \pm 0.000\,51$
i_b (°)	$\mathcal{U}(80, 90)$	84.44 ± 0.23	$87.40^{+1.75}_{-1.88}$
Photometry-related parameters			
$q_{1,\,K2-CHEOPS}$	$\mathcal{U}(0, 1)$	$0.34^{+0.24}_{-0.15}$	$0.36^{+0.31}_{-0.20}$
$q_{2,\,K2-CHEOPS}$	$\mathcal{U}(0, 1)$	$0.36^{+0.36}_{-0.26}$	$0.25^{+0.32}_{-0.18}$
$q_{1,\,TESS}$	$\mathcal{U}(0, 1)$	$0.15^{+0.23}_{-0.11}$	$0.22^{+0.31}_{-0.15}$
$q_{2,\,TESS}$	$\mathcal{U}(0, 1)$	$0.40^{+0.38}_{-0.28}$	$0.31^{+0.37}_{-0.22}$
Stellar parameters			
$\rho_\star[\rho_\odot]$	$\mathcal{G}(1.14, 0.06)$	1.14 ± 0.06	1.13 ± 0.06
Acceleration, $\dot{\gamma}$ ($m\,s^{-1}d^{-1}$)	$\mathcal{U}(-1, 1)$	0.007 ± 0.039	0.006 ± 0.040
Instrument-related parameters			
$\sigma_{jit,\,HARPS-N}$ ($m\,s^{-1}$)	$\mathcal{U}(0, 50)$	$1.8^{+1.2}_{-1.1}$	$1.1^{+1.0}_{-0.7}$
$\gamma_{HARPS-N}$ ($m\,s^{-1}$)	$\mathcal{U}(-22\,500, -21\,900)$	$-22\,122.9^{+26.2}_{-25.8}$	$-22\,122.9^{+26.6}_{-26.9}$
$\sigma_{jit,\,HARPS}$ ($m\,s^{-1}$)	$\mathcal{U}(0, 50)$	$0.8^{+0.8}_{-0.5}$	$0.7^{+0.8}_{-0.5}$
γ_{HARPS} ($m\,s^{-1}$)	$\mathcal{U}(-22\,100, -21\,800)$	$-21\,977.5 \pm 40.1$	$-21\,976.5^{+42.3}_{-40.8}$
$\sigma_{jit,\,K2}$ (normal flux)	$\mathcal{U}(0, 0.1)$	$0.000\,001 \pm 0.000\,001$	$0.000\,001^{+0.000\,002}_{-0.000\,001}$
$\sigma_{jit,\,TESS}$ (normal flux)	$\mathcal{U}(0, 0.1)$	$0.000\,07^{+0.000\,06}_{-0.000\,05}$	$0.000\,07^{+0.000\,07}_{-0.000\,05}$
$\sigma_{jit,\,CHEOPS}$ (normal flux)	$\mathcal{U}(0, 0.1)$	$0.0004 \pm 0.000\,04$	0.0004 ± 0.00003
Derived parameters			
Semimajor axis, a_b (au)		$0.032\,10^{+0.000\,40}_{-0.000\,43}$	$0.032\,10^{+0.000\,40}_{-0.000\,43}$
Mass, m_b ($M_\oplus$)		$11.1^{+1.5}_{-1.4}$	11.1 ± 1.4
Radius, r_b [$R_\oplus$]		2.67 ± 0.05	2.52 ± 0.06
Mean density, ρ_b ($g\,cm^{-3}$)		$3.2^{+0.5}_{-0.4}$	$3.8^{+0.6}_{-0.5}$
Eccentricity, e_b		0 (fixed)	$0.31^{+0.04}_{-0.06}$
Periastron argument, $\omega_{\star,\,b}$ (rad)		$\pi/2$ (fixed)	1.49 ± 0.22
$T_{peri,\,b}$ (BJD-2450000)		–	$7860.705^{+0.038}_{-0.039}$
Impact parameter		0.71 ± 0.03	$0.23^{+0.20}_{-0.16}$
Transit duration (d)		$0.0698^{+0.0032}_{-0.0031}$	0.0676 ± 0.0022
Limb-darkening coeff. 1, $u_{1,\,K2-CHEOPS}$		$0.41^{+0.33}_{-0.28}$	$0.29^{+0.24}_{-0.19}$
Limb-darkening coeff. 2, $u_{2,\,K2-CHEOPS}$		$0.16^{+0.36}_{-0.38}$	$0.29^{+0.33}_{-0.35}$
Limb-darkening coeff. 1, $u_{1,\,TESS}$		$0.27^{+0.30}_{-0.19}$	$0.26^{+0.29}_{-0.18}$
Limb-darkening coeff. 2, $u_{2,\,TESSS}$		$0.06^{+0.29}_{-0.21}$	$0.14^{+0.36}_{-0.26}$
Bayesian evidence, $\ln \mathcal{Z}$		66 192.5	66 195.0

[a]The uncertainties are given as the 16th and 84th percentiles of the posterior distributions.

Downloaded from https://academic.oup.com/mnras/article/535/1/531/7819156 by Uni PD user on 04 September 2025

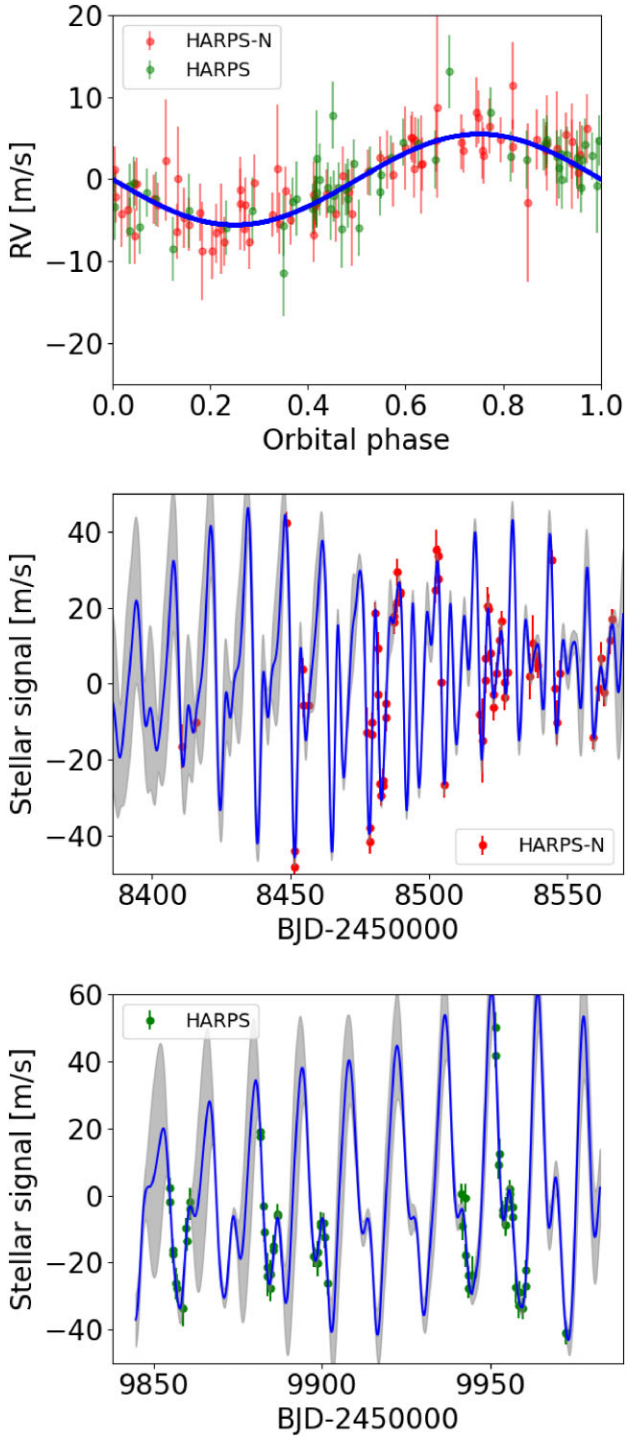

Figure 8. Top panel: phase-folded best-fitting orbital model for the transiting companion K2-370 b (blue curve). Red- and green-filled circles correspond to HARPS-N and HARPS observations, respectively. Center panel: example of HARPS-N RVs activity signal (after subtracting the $e = 0$ planetary signal), modelled by the GP regression parameters in Table 2. The error bars include the uncorrelated jitter terms added in quadrature to the formal RV uncertainties. Bottom panel: the same, but for a section of the HARPS RVs.

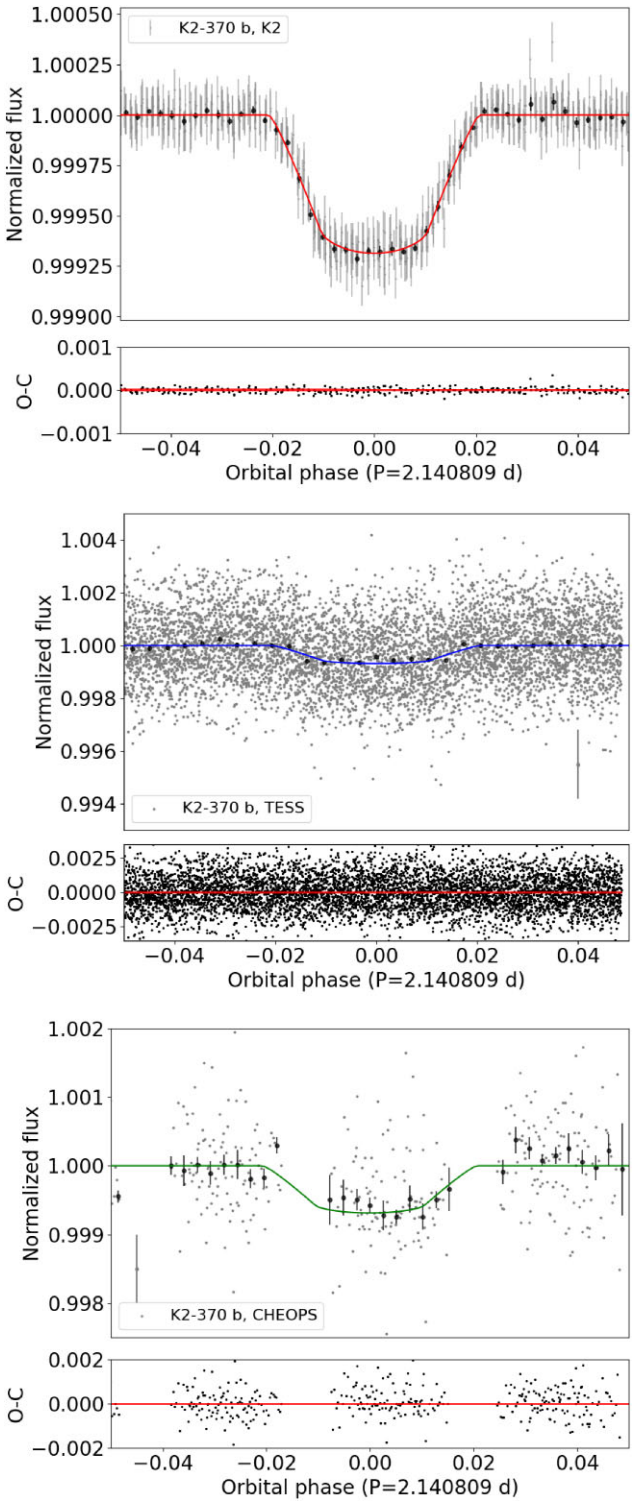

Figure 9. Top panel: phase-folded K2 transit light curve of K2-370 b and post-fit residuals. The best-fitting transit model produced in the combined RV + photometry data analysis in Section 3.4 is depicted by the red curve. The black dots represent data averaged over 6.9 min bins. Center panel: the same for the *TESS* photometry. The best-fitting model is depicted by the blue curve. The black dots represent data averaged over 10.3 min bins. Bottom panel: the same for the CHEOPS photometry. The best-fitting model is depicted by the green curve. The black dots represent data averaged over 6.2 min bins.

Downloaded from https://academic.oup.com/mnras/article/535/1/531/7819156 by Uni PD user on 04 September 2025

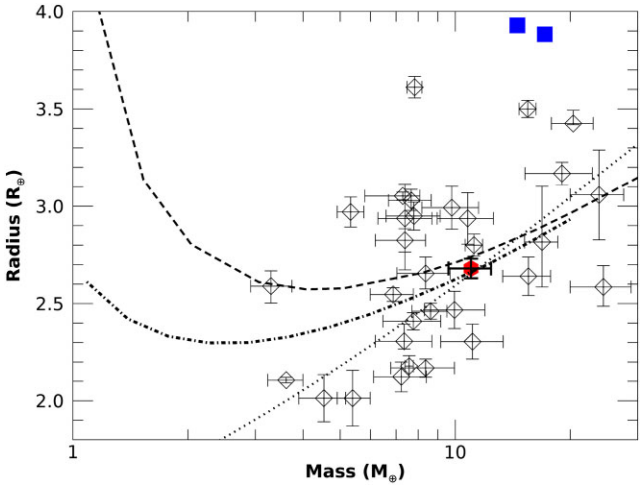

Figure 10. Mass–radius diagram of sub-Neptunes with masses $\leq 30\,M_\oplus$ detected at the 5σ level (or better), including K2-370 b (red hexagon), orbiting primaries with $T_{\rm eff} > 5500$ K. The different curves depict internal structure models of variable composition: a pure water world with 100 per cent H_2O layer by mass (dotted line) or a planet with an Earth-like rocky core (98 per cent) + 2 per cent H_2 envelope by mass (dashed line) from Zeng et al. (2019), and an ocean planet with a core to core + mantle mass fraction of 40 per cent and a total water mass fraction of 40 per cent at an irradiation temperature of 1300 K (dashed–dotted line) from Aguichine et al. (2021). The location of Uranus and Neptune is also indicated (blue squares). Data of transiting systems used for this and the following plot are taken from the TEPCat catalogue as of 2024 August.

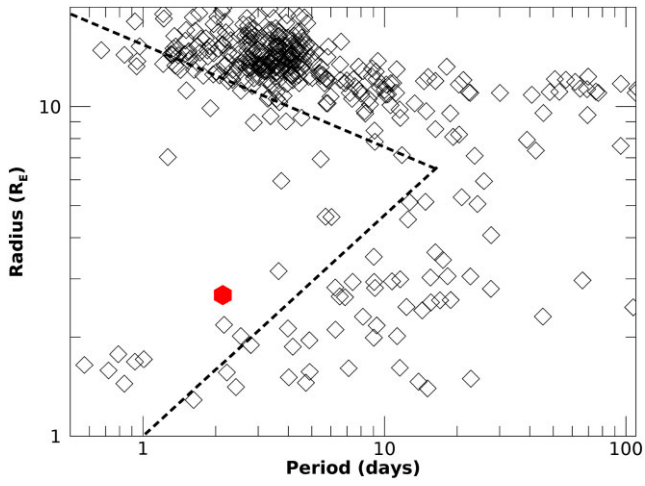

Figure 11. Radius as a function of orbital period for transiting planets with masses and radii measured at the 5σ and 10σ level (or better), respectively, including K2-370 b (filled hexagon), orbiting primaries with $T_{\rm eff} > 5500$ K. The thick long-dashed lines identify the approximate upper and lower boundaries of the hot Neptune desert (Mazeh et al. 2016).

those from the combined RV + photometry analysis, within their formal uncertainties.

4 DISCUSSION

4.1 K2-370 b's structural properties

Even in the presence of dominant stellar activity RV variations, the Doppler signal of K2-370 b ($K_{\rm b} = 5.6 \pm 0.7\,{\rm m\,s^{-1}}$) is recovered with high precision, at $\simeq 8\sigma$ level. We derive a mass $M_{\rm b} = 11.1 \pm 1.4\,M_\oplus$, a radius $R_{\rm b} = 2.67 \pm 0.05\,R_\oplus$, and a planetary mean density $\rho_{\rm b} = 3.2 \pm 0.4\,{\rm g\,cm^{-3}}$. In the mass–radius diagram[8] (Fig. 10) of sub-Neptunes orbiting G- and F-type primaries ($T_{\rm eff} > 5500$ K) with mass and radius determined to better than 20 and 10 per cent, respectively, K2-370 b sits at the approximate boundary between the sub-sample of companions with typically smaller radius whose interior structure can still be described by models that do not require the presence of a Hydrogen-dominated gaseous envelope and the sub-sample of companions with typically larger radius for which instead the presence of an H_2 envelope must be invoked. Indeed (see Fig. 10), K2-370 b's composition could be described as corresponding to an ~ 100 per cent water world with no H_2-rich atmosphere (Zeng et al. 2019), or a massive rocky planet surrounded by a H_2-dominated envelope of ~ 2 per cent by mass (Zeng et al. 2019). The planet's mass and radius also fit the definition of an irradiated ocean planet with a significant water mass fraction (~ 40 per cent) in supercritical steam state, and thus with an H_2O-dominated atmosphere (e.g. Aguichine et al. 2021). The well-known degeneracies in composition that particularly affect sub-Neptunes with radii in the range $2-3\,R_\oplus$ therefore do not allow to provide a clear picture of K2-370 b's internal structure, and additional constraints must be sought for, as we detail below.

4.2 K2-370 b's evolutionary history

In a radius-orbital period diagram populated by transiting planets with well-measured properties around dwarf stars with $T_{\rm eff} > 5500$ K (Fig. 11), K2-370 b is highlighted as the sub-Neptune with the shortest period, and the second-hottest companion with radius in the $2 - 4\,R_\oplus$ range (the recently discovered sub-Neptune TOI-1408 c has an inferred $T_{\rm eq} \sim 2000$ K, as reported by Korth et al. 2024). If we take the approximate boundaries of the hot Neptune desert (Szabó & Kiss 2011; Mazeh, Holczer & Faigler 2016) between ~ 2 and $\sim 10 R_\oplus$ and $P \lesssim 3$ d, then K2-370 b sits just inside its lower boundary.

We simulated the evaporation history of K2-370 b to determine whether the intense X-ray irradiation the planet has received in the past is consistent with the presence of a H/He-rich atmosphere. To do so, we first modelled its internal structure assuming it is comprised of a rocky core surrounded by a pure H/He atmosphere. We combined the mass–radius relation by Otegi, Bouchy & Helled (2020b), to determine the mass ($M_{\rm core}$) and radius ($R_{\rm core}$) of the rocky core, together with the envelope structure model by Chen & Rogers (2016), which ties the thickness of the atmosphere $R_{\rm env}$ (and its temperature) to the envelope mass fraction $f_{\rm env}$, defined as the ratio of envelope to planet mass. We thus determined an envelope mass fraction of 0.50 ± 0.15 per cent and an envelope thickness of $0.62 \pm 0.12\,R_\oplus$.

We then simulated the evaporation history of the planet with the `photoevolver` code (Fernández Fernández, Wheatley & King 2023). In order to determine the evolution of the planet's atmosphere under evaporation, knowledge of the stellar X-ray emission history is required. Since the X-ray activity of a star is tied to its spin period, where faster rotators are X-ray brighter (e.g. Pizzolato et al. 2003; Wright et al. 2011), we can use models of the rotational evolution of stars to estimate their X-ray emission across their lifetime. We adopted the rotational evolution models by Johnstone et al. (2021), which predicted a gyrochronological age of 1.4 ± 0.4 Gyr for K2-

[8]Data from the transiting exoplanet catalogue TEPC at: https://www.astro.keele.ac.uk/jkt/tepcat/

Downloaded from https://academic.oup.com/mnras/article/535/1/531/7819156 by Uni PD user on 04 September 2025

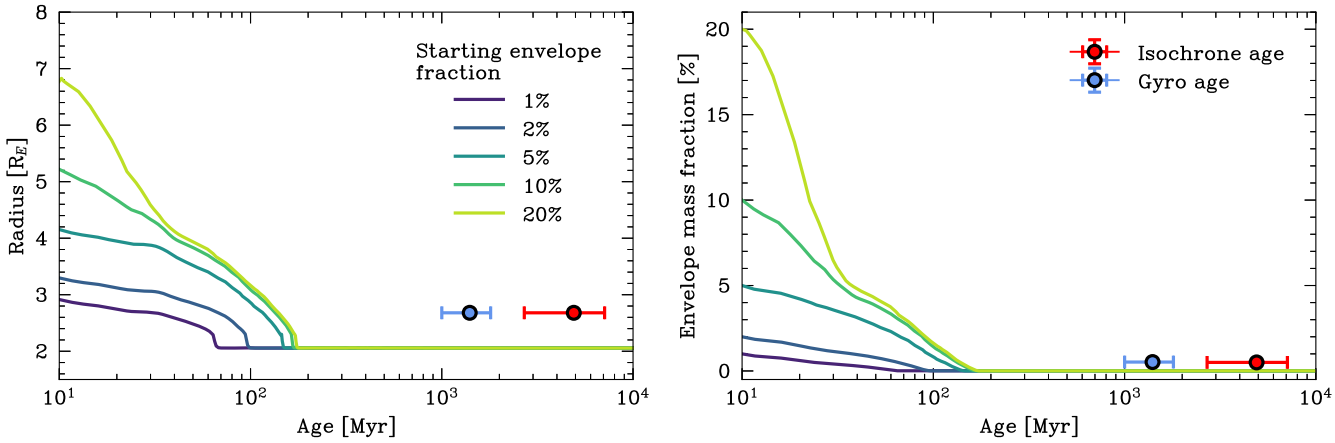

Figure 12. Evaporation histories of K2-370 b with a range of initial envelope mass fractions, showing the evolution of the radius (left panel) and envelope mass fraction (right panel). The age determined from isochrone fitting is shown as a red circle, and the gyrochronology estimate as a blue circle.

370. This estimate is somewhat in tension with the age of 5 ± 2 Gyr determined from isochrone fitting (see Section 3.1). For that reason, we consider both ages in our analysis.

We also adopted the mass-loss model by Kubyshkina et al. (2018) to determine the evaporation rate from the planet from its incident XUV irradiation. This model also predicted a present-day mass-loss rate of $(3.5 \pm 1.0) \times 10^{10}$ g s^{-1}.

We thus evolved the planet's atmosphere under photoevaporation from the age of 10 Myr to 10 Gyr, using a range of initial envelope mass fractions from 1 to 20 per cent placed on to the rocky core. We adopted the fourth-order Runge–Kutta algorithm as the integration method, provided with the PYTHON package SCIPY (Virtanen et al. 2020), with an adaptive step size no larger than 1 Myr. The results, shown on Fig. 12, indicate that all scenarios yield a planet completely stripped of its H/He atmospheres before the age of 180 Myr, far earlier than the age estimates for K2-370. This implies the planet's present-day structure is thus inconsistent with a pure H/He envelope.

4.3 Limits to the presence of outer companions

We also tested for the presence of additional non-transiting companions, by deriving the detection limits from the combined RV data set. To compute the detection limits, we performed injection-recovery simulations, similar to those performed in Bonomo et al. (2023) and Naponiello et al. (2023), with the following modifications: To correctly take into account the effects of stellar activity in the detection of additional companions in the RVs, we injected the simulated signals into the actual RV data, after correcting for instrumental offsets, and then tested the recovery by comparing the BIC of the final RV model, including all the relevant terms from the best-fitting model (see Table 2), to that of a model including also the simulated planetary signal. In this way the GP regression is included in the analysis, and the effects of stellar activity are taken into account. We performed this analysis in a logarithmic grid of 50×100 in minimum mass and orbital period, respectively, covering the ranges [1, 1000] $M_\oplus$ and [0.5, 5000] d.

The resulting detection map is shown in Fig. 13. It is worth noticing that, due to the correct modelling of the stellar activity by the inclusion of the GP, the detection functions drops near the stellar rotation period, $\theta \simeq 13.5$ d, and its harmonics, $\theta/2$, $\theta/3$. The detection map shows that, given the high activity levels of the primary, with this data set it is currently impossible to reveal the presence of additional sub-

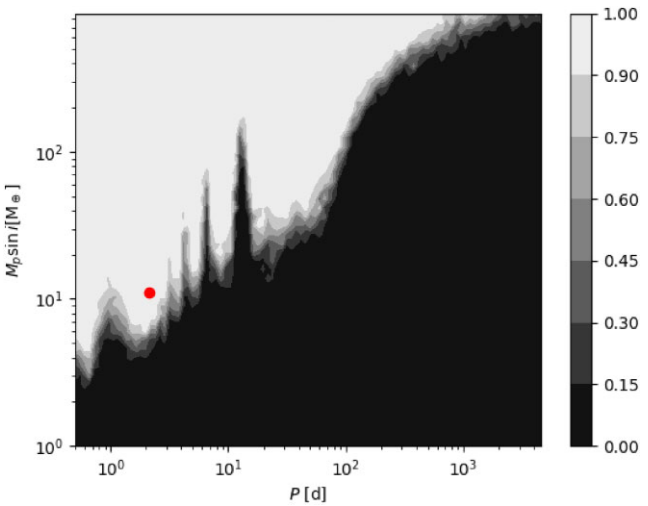

Figure 13. Map of the detection limits of the HARPS-N + HARPS RV time-series of K2-370. The colour-scale shows the detection probability of additional companions in the period–minimum mass space. The filled dot marks the position of K2-370 b.

Neptune-type companions ($M_p \sin i \lesssim 20 M_\oplus$) for $P \gtrsim 10$ d. In the approximate separation range 1−5 au, we would have instead been sensitive to the presence of giant planets with $M_p \sin i \simeq 1-3 M_{Jup}$. An additional, although looser, constraint on the presence of long-period companions can be obtained by *Gaia* DR3 astrometry. Based on a numerical evaluation of the *Gaia* DR3 sensitivity to orbiting companions centred on the observed Renormalized Unit Weight Error value of 0.99 for K2-370 (see e.g. Blanco-Pozo et al. 2023; Suárez Mascareño et al. 2023), only companions in the approximate $10-50\,M_{Jup}$ mass range can be ruled out in the same separation interval.

4.4 Prospects for atmospheric characterization

Based on K2-370 b's mass, radius, and T_{eq}, and the primary radius estimate, we can use standard metrics (Kempton et al. 2018) to gauge the prospects for successful atmospheric characterization measurements both in transmission and emission with *JWST*, We obtain a transmission spectroscopy metric of ~ 43 and an emission

Downloaded from https://academic.oup.com/mnras/article/535/1/531/7819156 by Uni PD user on 04 September 2025

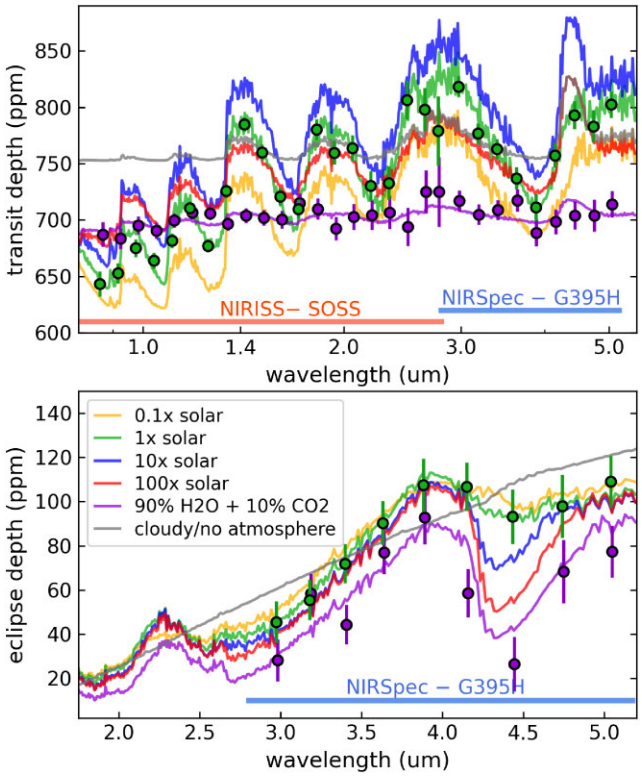

Figure 14. *JWST* simulations of K2-370 b of transit (top panel) and eclipse (bottom panel) observations. The solid curves show synthetic spectra of K2-370 b assuming a range of atmospheric compositions (see legend in bottom panel). The grey curve on the top (transit) shows a 100x solar scenario with a grey cloud deck at 0.1 mbar, whereas the grey model at the bottom (eclipse) shows a blackbody scenario. The markers with error bars show the noised up observations for two-selected atmospheric scenarios, as observed with the instrumental/detector configuration labelled at the bottom of the panels. The error bars denote accumulated SNRs expected for a total of three observations with each instrument.

spectroscopy metric (ESM) of ~ 7.5, lower than the estimates from Christiansen et al. (2022) due to the revised planetary radius. Due to K2-370 b's high equilibrium temperature, its ESM value indicates emission spectroscopy with *JWST* might provide interesting constraints.

To estimate the transmission and emission spectral signals from K2-370 b as observed by *JWST*, we computed synthetic spectra using the open-source PYRAT BAY modelling framework (Cubillos & Blecic 2021). We modelled a 1D cloud-free atmosphere in radiative and thermochemical equilibrium (Cubillos et al., in preparation), simulating a broad range of elemental compositions to explore from H-dominated to secondary atmospheres. For the thermochemical-equilibrium calculations, we considered a set of 45 neutral and ionic species, whereas for the radiative-transfer calculations we considered opacities from molecular species for CO, CO_2, CH_4, H_2O, HCN, NH_3, and C_2H_2 from HITEMP and ExoMol (Rothman et al. 2010; Tennyson et al. 2016); Na and K resonant lines (Burrows, Marley & Sharp 2000); H, H_2, and He Rayleigh (Kurucz 1970); and H_2–H_2 and H_2–He collision-induced absorption (Borysow, Jorgensen & Fu 2001; Borysow 2002; Richard et al. 2012). We pre-processed the large ExoMol line lists with the REPACK algorithm (Cubillos 2017) to extract the dominant transitions. Fig. 14 shows the model transit and eclipse spectra along with simulated *JWST* observations considering three observations per instrument using the Pandeia engine (Pontoppidan et al. 2016).

For transmission spectra characterization (Fig. 14, top panel), the 0.8–5.0-μm window offers the optimal combination of SNR and spectral features (mainly from H_2O and CO_2), with NIRSpec/G395H and NIRISS/SOSS being two ideal instrument to probe this spectral region. Hydrogen-dominated atmospheres with varying degrees of metal-element enhancements could be readily distinguished from each other. On the other hand, models with high metallicities (above $\sim 100\times$ solar) or secondary atmospheres (e.g. H_2O dominated) present featureless spectra that do not allow to distinguish their specific compositions. As noted in previous studies, clouds and hazes can mute spectral features, which complicates the interpretation of the observed spectra (e.g. Line & Parmentier 2016; Brande et al. 2024). We depicted one of these scenarios by adding a grey cloud deck at 0.1 mbar for the 100x solar metallicity model (compare the red and grey models in the top panel of Fig. 14). While clouds largely flatten a transmission spectrum, different condensates have coarse by distinctive spectral features. A broad enough spectral coverage such as that achievable with *JWST* may still be able to constrain exoplanet atmospheres in the presence of clouds (see e.g. Dyrek et al. 2024).

For emission spectra characterization (Fig. 14, bottom panel), we found that at wavelengths shorter than 3 μm the planetary signal is too weak to distinguish between different models, whereas at wavelengths longer than 5 μm most spectral features look similar for all scenarios. In contrast, the 2.8–5.2- μm window, observable with NIRSpec/G395H, has the optimal potential for characterization due to the strong CO_2 feature at 4.4 μm, which varies significantly for each model. While a precise abundance determination would still be challenging, we expect that *JWST* emission observations at these wavelengths should be able to distinguish between the most extreme scenarios of a H-dominated atmosphere, a secondary atmosphere, or a blackbody emission (no atmosphere). As in transmission, the presence of clouds would flatten the emission spectral features toward a more blackbody-like spectrum whose brightness temperature is dictated by the albedo, optical and infrared mean opacities, and dynamics of the atmosphere.

5 CONCLUSIONS

K2-370 b joins a growing sample of some 30 sub-Neptunes orbiting F- and G-type dwarfs with well-constrained masses and radii. The mass distribution of these companions populating the second peak of the size distribution has median $7.8\,M_\oplus$ and standard deviation $5.5\,M_\oplus$ (see Fig. 15). It is dominated by a cluster of ~ 70 per cent of the objects distributed between ~ 4 and $\sim 11\,M_\oplus$, with a narrow peak of ~ 30 per cent of companions with masses between ~ 7 and $\sim 8\,M_\oplus$. K2-370 b sits at the high-mass end of the cluster. The present-day range of observed properties of these close-in sub-Neptunes can be understood within the context of the combined effect of formation and mass-loss mechanisms (e.g. Venturini et al. 2020, and references therein). To explain the properties of the subset (~ 20 per cent) of higher mass companions, with M_p in the range $15-25\,M_\oplus$, additional mechanisms likely have been at work, which prevented gas accretion and/or enhanced mass-loss.

The mass of K2-370 b, $M_p = 11.1 \pm 1.4\,M_\oplus$, straddles the threshold for runaway accretion of solids and consequent giant planet formation (e.g. Raymond & Morbidelli 2022, and references therein). As a member of the population of close-in sub-Neptunes, K2-370 b likely escaped evolution into a gas giant through pathways possibly involving the formation of a large, ice-rich core beyond the snowline and its subsequent inward migration or the growth of

Downloaded from https://academic.oup.com/mnras/article/535/1/531/7819156 by Uni PD user on 04 September 2025

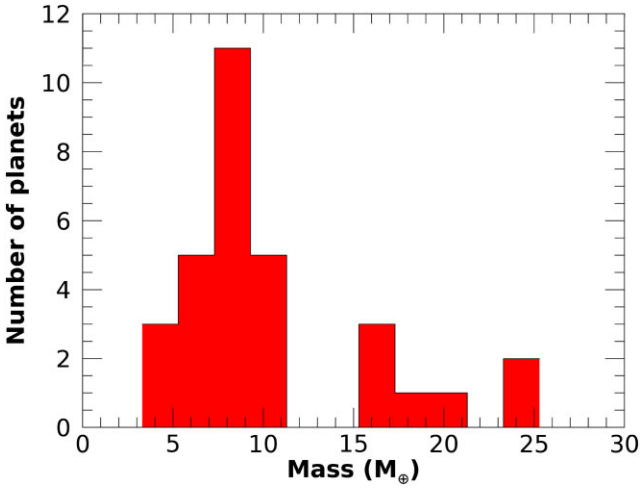

Figure 15. Histogram of the mass distribution of the sample of sub-Neptunes shown in Fig. 10.

a large, rocky core in the inner part of the disc assembled from inward-drifting pebbles (for a review of the two mechanisms, see e.g. Bean et al. 2021). The strong irradiation levels to which the planet is subjected imply, as we have seen (Section 4.2), that in the event of an early arrival of the planet at its present location any significant gaseous envelope collected in the process might be lost by now, even in the case of the system being $\sim$ 1 Gyr of age. Its low density would then favour an ice-rich compositional scenario. Finding evidence of the presence of an H-dominated atmosphere might call for an alternative evolutionary path in which K2-370 b arrived quite recently at 0.03 au from its parent star. One such possibility might be realised via a secular migration scenario (Wu & Lithwick 2011; Petrovich, Deibert & Wu 2019), in which chaotic behaviour in a multiple system with moderate eccentricities and inclinations over long time-scales (up to a significant fraction of a Gyr) leads the innermost planet's orbit to become very eccentric, followed by tidal capture at very short orbital separation. In this case, we would be observing K2-370 b shortly after the secular migration event has occurred (Myr time-scale), which would explain any still-existing gas envelope (yet to be fully eroded as the process was triggered only recently) and the tentative evidence for a not fully circularized orbit. A further consequence would be the likely significant misalignment between the stellar spin axis and the normal to the planetary orbit (obliquity). It is worth noting that, in addition to the better established observational evidence on the obliquity distribution collected for hot Jupiters (e.g. Albrecht, Dawson & Winn 2022; Hamer & Schlaufman 2022; Morgan et al. 2024), highly misaligned (even polar) orbits for hot and warm Neptune-type planets at the edge of the desert, effectively resistant against tidal dissipation and re-alignment, are not uncommon (e.g. Bourrier et al. 2018, 2023). Given the parameters in Table 2 for the circular orbit case, the expected amplitude of the Rossiter–McLaughlin effect (e.g. Triaud 2018, and references therein) is $\sim 1.6\,\mathrm{m\,s^{-1}}$, a small value indeed but that might be within reach of an instrument such as ESPRESSO.

In conclusion, the above considerations further stress the need for additional follow-up characterization measurements for K2-370 b, through the identification of the basic composition of its atmosphere (or lack thereof), detection of still ongoing atmospheric escape using the metastable near-infrared ($\lambda = 1083.3$ nm) helium triplet diagnostic (e.g. Seager & Sasselov 2000; Oklopčić & Hirata 2018), and via determination of the degree of spin-orbit (mis)alignment, challenging as these observations might be. Finally, the future *Gaia* data releases, DR4 and DR5, will likely improve the constraints on the existence of higher mass, long-period companions, but long-term RV monitoring from the ground is also strongly encouraged.

ACKNOWLEDGEMENTS

An anonymous reviewer provided insightful comments that helped improving an earlier version of the manuscript. This paper includes data collected by the *TESS* mission. Funding for the *TESS* mission is provided by the NASA Explorer Program. We acknowledge the use of public TOI Release data from pipelines at the *TESS* Science Office and at the *TESS* Science Processing Operations Center. Resources supporting this work were provided by the NASA High-End Computing (HEC) Program through the NASA Advanced Supercomputing (NAS) Division at Ames Research Center for the production of the SPOC data products. This work has made use of data from the European Space Agency (ESA) mission *Gaia* (https://www.cosmos.esa.int/gaia), processed by the *Gaia* Data Processing and Analysis Consortium (DPAC, https://www.cosmos.esa.int/web/gaia/dpac/consortium). Funding for the DPAC has been provided by national institutions, in particular, the institutions participating in the *Gaia* Multilateral Agreement. We acknowledge financial contribution from the agreement ASI-INAF n.2018-16-HH.0. We gratefully acknowledge support from the Italian Space Agency (ASI) under contract 2018-24-HH.0 'The Italian participation to the Gaia Data Processing and Analysis Consortium (DPAC)' in collaboration with the Italian National Institute of Astrophysics. AVF acknowledges the support of the IOP through the Bell Burnell Graduate Scholarship Fund. ACC acknowledges support from STFC consolidated grant number ST/V000861/1, and UKSA grant number ST/X002217/1. This work has been carried out within the framework of the NCCR PlanetS supported by the Swiss National Science Foundation under grants 51NF40_182901 and 51NF40_205606. XD acknowledges the support from the European Research Council (ERC) under the European Union's Horizon 2020 research and innovation programme (grant agreement SCORE No 851555) and from the Swiss National Science Foundation under the grant SPECTRE (No 200021_215200). FPE would like to acknowledge the Swiss National Science Foundation (SNSF) for supporting research with HARPS-N through the SNSF grants nos. 140649, 152721, 166227, 184618, and 215190. This research was funded in part by the UKRI (grants ST/X001121/1 and EP/X027562/1). The HARPS-N Instrument Project was partially funded through the Swiss ESA-PRODEX Programme. CHEOPS is an ESA mission in partnership with Switzerland with important contributions to the payload and the ground segment from Austria, Belgium, France, Germany, Hungary, Italy, Portugal, Spain, Sweden, and the United Kingdom. The CHEOPS Consortium would like to gratefully acknowledge the support received by all the agencies, offices, universities, and industries involved. Their flexibility and willingness to explore new approaches were essential to the success of this mission. This research has made use of the Exoplanet Follow-up Observation Program (ExoFOP; DOI: 10.26134/ExoFOP5) website, which is operated by the California Institute of Technology, under contract with the National Aeronautics and Space Administration under the Exoplanet Exploration Program.

Downloaded from https://academic.oup.com/mnras/article/535/1/531/7819156 by Uni PD user on 04 September 2025

DATA AVAILABILITY

The K2 and *TESS* data underlying this article are publicly available and stored on the Mikulski Archive for Space Telescopes at https://archive.stsci.edu/k2/ and https://archive.stsci.edu/tess/, respectively. All CHEOPS data presented here are available from the CHEOPS mission archive (https://cheops.unige.ch/archive_browser/. Radial velocities from HARPS-N and HARPS are included in the tables found in the appendix.

REFERENCES

Adams E. R., Seager S., Elkins-Tanton L., 2008, ApJ, 673, 1160
Aguichine A., Mousis O., Deleuil M., Marcq E., 2021, ApJ, 914, 84
Albrecht S. H., Dawson R. I., Winn J. N., 2022, PASP, 134, 082001
Aller A., Lillo-Box J., Jones D., Miranda L. F., Barceló Forteza S., 2020, A&A, 635, A128
Ambikasaran S., Foreman-Mackey D., Greengard L., Hogg D. W., O'Neil M., 2015, IEEE Trans. Pattern Anal. Mach. Intell., 38, 2
Anna John A. A., Collier Cameron A., Wilson T. G., 2022, MNRAS, 515, 3975
Anna John A. et al., 2023, MNRAS, 525, 1687
Bailer-Jones C. A. L., Rybizki J., Fouesneau M., Demleitner M., Andrae R., 2021, AJ, 161, 147
Batalha N. E., Lewis T., Fortney J. J., Batalha N. M., Kempton E., Lewis N. K., Line M. R., 2019, ApJ, 885, L25
Bean J. L., Raymond S. N., Owen J. E., 2021, J. Geophys. Res. (Planets), 126, e06639
Benneke B. et al., 2019, ApJ, 887, L14
Benz W. et al., 2021, Exp. Astron., 51, 109
Berger T. A., Huber D., Gaidos E., van Saders J. L., Weiss L. M., 2020, AJ, 160, 108
Berta Z. K. et al., 2012, ApJ, 747, 35
Bitsch B., Raymond S. N., Izidoro A., 2019, A&A, 624, A109
Bitsch B., Raymond S. N., Buchhave L. A., Bello-Arufe A., Rathcke A. D., Schneider A. D., 2021, A&A, 649, L5
Blanco-Pozo J. et al., 2023, A&A, 671, A50
Bodenheimer P., Lissauer J. J., 2014, ApJ, 791, 103
Bonomo A. S. et al., 2023, A&A, 677, A33
Borysow A., 2002, A&A, 390, 779
Borysow A., Jorgensen U. G., Fu Y., 2001, J. Quant. Spec. Radiat. Transf., 68, 235
Bourrier V. et al., 2018, Nature, 553, 477
Bourrier V. et al., 2023, A&A, 669, A63
Brande J. et al., 2024, ApJ, 961, L23
Brown D. J. A., 2014, MNRAS, 442, 1844
Buchhave L. A. et al., 2012, Nature, 486, 375
Buchhave L. A. et al., 2014, Nature, 509, 593
Buchner J. et al., 2014, A&A, 564, A125
Burrows A., Marley M. S., Sharp C. M., 2000, ApJ, 531, 438
Cadieux C. et al., 2024, ApJ, 960, L3
Castro-González A. et al., 2023, A&A, 675, A52
Chen J., Kipping D., 2017, ApJ, 834, 17
Chen H., Rogers L. A., 2016, ApJ, 831, 180
Christiansen J. L. et al., 2022, AJ, 163, 244
Collier Cameron A. et al., 2021, MNRAS, 505, 1699
Colman I. L., Angus R., David T., Curtis J., Hattori S., Lu Y. L., 2024, AJ, 167, 189
Cosentino R. et al., 2012, in McLean I. S., Ramsay S. K., Takami H., eds, SPIE Conf. Ser. Vol. 8446, Ground-based and Airborne Instrumentation for Astronomy IV. SPIE, Bellingham, p. 84461V
Crossfield I. J. M., Kreidberg L., 2017, AJ, 154, 261
Cubillos P. E., 2017, ApJ, 850, 32
Cubillos P. E., Blecic J., 2021, MNRAS, 505, 2675
Cutri R. M. et al., 2014, VizieR Online Data Catalog. p. II/328, Available at: https://ui.adsabs.harvard.edu/abs/2014yCat.2328....0C
Cutri R. M. et al., 2003, VizieR Online Data Catalog. p. II/246, Available at: https://ui.adsabs.harvard.edu/abs/2003yCat.2246....0C
Donahue R. A., 1998, in Donahue R. A., Bookbinder J. A., eds, ASP Conf. Ser. Vol. 154, Cool Stars, Stellar Systems, and the Sun. Astron. Soc. Pac., San Francisco. p. 1235
Dotter A., 2016, ApJS, 222, 8
Dotter A., Chaboyer B., Jevremović D., Kostov V., Baron E., Ferguson J. W., 2008, ApJS, 178, 89
Dymont A. H., Yu X., Ohno K., Zhang X., Fortney J. J., Thorngren D., Dickinson C., 2022, ApJ, 937, 90
Dyrek A. et al., 2024, Nature, 625, 51
Edelson R. A., Krolik J. H., 1988, ApJ, 333, 646
Edwards B. et al., 2023, ApJS, 269, 31
Espinoza N., Kossakowski D., Brahm R., 2019, MNRAS, 490, 2262
Estrela R., Swain M. R., Roudier G. M., 2022, ApJ, 941, L5
Evans D. W. et al., 2018, A&A, 616, A4
Faria J. P., Santos N. C., Figueira P., Brewer B. J., 2018, J. Open Source Softw., 3, 487
Fernández Fernández J., Wheatley P. J., King G. W., 2023, MNRAS, 522, 4251
Feroz F., Hobson M. P., Cameron E., Pettitt A. N., 2019, Open J. Astrophys., 2, 10
Foreman-Mackey D., Hogg D. W., Lang D., Goodman J., 2013, PASP, 125, 306
Foreman-Mackey D., Agol E., Ambikasaran S., Angus R., 2017, AJ, 154, 220
Fortney J. J., Mordasini C., Nettelmann N., Kempton E. M. R., Greene T. P., Zahnle K., 2013, ApJ, 775, 80
Fulton B. J., Petigura E. A., 2018, AJ, 156, 264
Fulton B. J. et al., 2017, AJ, 154, 109
Gaia Collaboration et al., 2021, A&A, 649, A1
Gaia Collaboration et al., 2023, A&A, 674, A1
Gao P. et al., 2023, ApJ, 951, 96
Ginzburg S., Schlichting H. E., Sari R., 2018, MNRAS, 476, 759
Guilluy G. et al., 2020, AJ, 161, 22
Guo X. et al., 2020, AJ, 159, 239
Gupta A., Schlichting H. E., 2019, MNRAS, 487, 24
Hamer J. H., Schlaufman K. C., 2022, AJ, 164, 26
Hansen B. M. S., Murray N., 2012, ApJ, 751, 158
Haywood R. D. et al., 2014, MNRAS, 443, 2517
Høg E. et al., 2000, A&A, 355, L27
Howell S. B. et al., 2014, PASP, 126, 398
Hoyer S., Guterman P., Demangeon O., Sousa S. G., Deleuil M., Meunier J. C., Benz W., 2020, A&A, 635, A24
Inamdar N. K., Schlichting H. E., 2016, ApJ, 817, L13
Izidoro A., Bitsch B., Raymond S. N., Johansen A., Morbidelli A., Lambrechts M., Jacobson S. A., 2021, A&A, 650, A152
Izidoro A., Schlichting H. E., Isella A., Dasgupta R., Zimmermann C., Bitsch B., 2022, ApJ, 939, L19
Jenkins J. M., 2002, ApJ, 575, 493
Jenkins J. M. et al., 2010, in Radziwill N. M., Bridger A., eds, SPIE Conf. Ser. Vol. 7740, Software and Cyberinfrastructure for Astronomy. SPIE, Bellingham. p. 77400D
Jenkins J. M. et al., 2016, SPIE Conf. Ser. Vol. 9913, Software and Cyberinfrastructure for Astronomy IV. p. SPIE, Bellingham, p. 99133E
Jin S., Mordasini C., 2018, ApJ, 853, 163
Johansen A., Lambrechts M., 2017, Annu. Rev. Earth Planet. Sci., 45, 359
Johnstone C. P., Bartel M., Güdel M., 2021, A&A, 649, A96
Kawashima Y., Ikoma M., 2019, ApJ, 877, 109
Kempton E. M. R. et al., 2018, PASP, 130, 114401
Kempton E. M. R. et al., 2023a, Nature, 620, 67
Kempton E. M. R., Lessard M., Malik M., Rogers L. A., Futrowsky K. E., Ih J., Marounina N., Muñoz-Romero C. E., 2023b, ApJ, 953, 57
Kipping D. M., 2010, MNRAS, 408, 1758
Knutson H. A. et al., 2014, ApJ, 794, 155
Korth J. et al., 2024, ApJ, 971, L28
Kreidberg L., 2015, PASP, 127, 1161
Kreidberg L. et al., 2014, Nature, 505, 69

Downloaded from https://academic.oup.com/mnras/article/535/1/531/7819156 by Uni PD user on 04 September 2025

Kreidberg L. et al., 2020, AJ, 164, 15
Kubyshkina D. et al., 2018, ApJ, 866, L18
Kurucz R. L., 1970, SAO Special Report, 309
Kurucz R. L., Smithsonian Astrophysical Observatory Cambridge, MA. 1993, SYNTHE Spectrum Synthesis Programs and Line Data.
Lee E. J., Chiang E., 2016, ApJ, 817, 90
Lee E. J., Connors N. J., 2021, ApJ, 908, 32
Lee E. J., Karalis A., Thorngren D. P., 2022, ApJ, 941, 186
Léger A. et al., 2004, Icarus, 169, 499
Li J., Tenenbaum P., Twicken J. D., Burke C. J., Jenkins J. M., Quintana E. V., Rowe J. F., Seader S. E., 2019, PASP, 131, 024506
Lillo-Box J. et al., 2020, A&A, 642, A121
Lindegren L. et al., 2021, A&A, 649, A2
Line M. R., Parmentier V., 2016, ApJ, 820, 78
Lomb N. R., 1976, Ap&SS, 39, 447
Lopez E. D., Fortney J. J., Miller N., 2012, ApJ, 761, 59
Lovis C. et al., 2011, preprint (arXiv:1107.5325)
Lozovsky M., Helled R., Dorn C., Venturini J., 2018, ApJ, 866, 49
Luger R., Barnes R., Lopez E., Fortney J., Jackson B., Meadows V., 2015, Astrobiology, 15, 57
Luque R., Pallé E., 2022, Science, 377, 1211
López-Morales M. et al., 2016, AJ, 152, 204
MacDonald M. G., Dawson R. I., Morrison S. J., Lee E. J., Khandelwal A., 2020, ApJ, 891, 20
Madhusudhan N., Nixon M. C., Welbanks L., Piette A. A. A., Booth R. A., 2020, ApJ, 891, L7
Madhusudhan N., Sarkar S., Constantinou S., Holmberg M., Piette A. A. A., Moses J. I., 2023, ApJ, 956, L13
Mamajek E. E., Hillenbrand L. A., 2008, ApJ, 687, 1264
Matsumura S., Takeda G., Rasio F. A., 2008, ApJ, 686, L29
Matsumura S., Peale S. J., Rasio F. A., 2010, ApJ, 725, 1995
Maxted P. F. L., Serenelli A. M., Southworth J., 2015, A&A, 577, A90
Maxted P. F. L. et al., 2022, MNRAS, 514, 77
Mazeh T., Holczer T., Faigler S., 2016, A&A, 589, A75
Mikal-Evans T. et al., 2023, AJ, 165, 84
Miller-Ricci E., Seager S., Sasselov D., 2009, ApJ, 690, 1056
Morgan M., Bowler B. P., Tran Q. H., Petigura E., Nagpal V., Blunt S., 2024, AJ, 167, 48
Mortier A., Santos N. C., Sousa S. G., Fernandes J. M., Adibekyan V. Z., Delgado Mena E., Montalto M., Israelian G., 2013, A&A, 558, A106
Mortier A., Sousa S. G., Adibekyan V. Z., Brandão I. M., Santos N. C., 2014, A&A, 572, A95
Mortier A. et al., 2020, MNRAS, 499, 5004
Mousis O., Deleuil M., Aguichine A., Marcq E., Naar J., Aguirre L. A., Brugger B., Gonçalves T., 2020, ApJ, 896, L22
Naponiello L. et al., 2023, Nature, 622, 255
Neil A. R., Liston J., Rogers L. A., 2022, ApJ, 933, 63
Noyes R. W., Hartmann L. W., Baliunas S. L., Duncan D. K., Vaughan A. H., 1984, ApJ, 279, 763
Oklopčić A., Hirata C. M., 2018, ApJ, 855, L11
Ormel C. W., Vazan A., Brouwers M. G., 2021, A&A, 647, A175
Otegi J. F., Bouchy F., Helled R., 2020a, A&A, 634, A43
Otegi J. F., Bouchy F., Helled R., 2020b, A&A, 634, A43
Owen J. E., Wu Y., 2017, ApJ, 847, 29
Petrovich C., Deibert E., Wu Y., 2019, AJ, 157, 180
Piaulet C. et al., 2023, Nat. Astron., 7, 206
Pizzolato N., Maggio A., Micela G., Sciortino S., Ventura P., 2003, A&A, 397, 147
Pontoppidan K. M. et al., 2016, in Peck A. B., Seaman R. L., Benn C. R.eds, SPIE Conf. Ser. Vol. 9910, Observatory Operations: Strategies, Processes, and Systems VI. SPIE, Bellingham, p. 991016
Raymond S. N., Morbidelli A., 2022, in Biazzo K., Bozza V., Mancini L., Sozzetti A., eds, Astrophysics and Space Science Library Vol. 466, Demographics of Exoplanetary Systems, Lecture Notes of the 3rd Advanced School on Exoplanetary Science. Springer-Verlag, Berlin. p. 3
Richard C. et al., 2012, J. Quant. Spec. Radiat. Transf., 113, 1276
Ricker G. R. et al., 2015, J. Astron. Telesc. Instrum. Syst., 1, 014003
Rogers L. A., 2015, ApJ, 801, 41
Rogers L. A., Seager S., 2010, ApJ, 712, 974
Rogers J. G., Schlichting H. E., Owen J. E., 2023, ApJ, 947, L19
Rothman L. S. et al., 2010, J. Quant. Spec. Radiat. Transf., 111, 2139
Roy P.-A. et al., 2023, ApJ, 954, L52
Saffe C., Gómez M., Chavero C., 2005, A&A, 443, 609
Scargle J. D., 1982, ApJ, 263, 835
Seager S., Sasselov D. D., 2000, ApJ, 537, 916
Smith J. C. et al., 2012, PASP, 124, 1000
Sousa S. G., 2014, Determination of Atmospheric Parameters of B-, A-, F- and G-Type Stars. Series: GeoPlanet: Earth and Planetary Sciences, Springer International Publishing, Cham, Switzerland, p. 297
Sousa S. G., Santos N. C., Israelian G., Mayor M., Udry S., 2011, A&A, 533, A141
Southworth J., 2011, MNRAS, 417, 2166
Sozzetti A., Torres G., Charbonneau D., Latham D. W., Holman M. J., Winn J. N., Laird J. B., O'Donovan F. T., 2007, ApJ, 664, 1190
Sozzetti A. et al., 2021, A&A, 648, A75
Speagle J. S., 2020, MNRAS, 493, 3132
Stumpe M. C. et al., 2012, PASP, 124, 985
Stumpe M. C., Smith J. C., Catanzarite J. H., Van Cleve J. E., Jenkins J. M., Twicken J. D., Girouard F. R., 2014, PASP, 126, 100
Suárez Mascareño A. et al., 2023, A&A, 670, A5
Szabó G. M., Kiss L. L., 2011, ApJ, 727, L44
Tennyson J. et al., 2016, J. Mol. Spectr., 327, 73
Triaud A. H. M. J., Springer International Publishing AG, 2018, in Deeg H. J., Belmonte J. A., eds, Handbook of Exoplanets. p. 2
Tsiaras A., Waldmann I. P., Tinetti G., Tennyson J., Yurchenko S. N., 2019, Nat. Astron., 3, 1086
Turbet M., Bolmont E., Ehrenreich D., Gratier P., Leconte J., Selsis F., Hara N., Lovis C., 2020, A&A, 638, A41
Twicken J. D. et al., 2018, PASP, 130, 064502
Valencia D., Guillot T., Parmentier V., Freedman R. S., 2013, ApJ, 775, 10
Van Eylen V., Agentoft C., Lundkvist M. S., Kjeldsen H., Owen J. E., Fulton B. J., Petigura E., Snellen I., 2018, MNRAS, 479, 4786
Vanderburg A., Johnson J. A., 2014, PASP, 126, 948
Vanderburg A. et al., 2016, ApJS, 222, 14
Venturini J., Guilera O. M., Haldemann J., Ronco M. P., Mordasini C., 2020, A&A, 643, L1
Virtanen P. et al., 2020, Nat. Methods, 17, 261
Wright N. J., Drake J. J., Mamajek E. E., Henry G. W., 2011, ApJ, 743, 48
Wu Y., Lithwick Y., 2011, ApJ, 735, 109
Wyatt M. C., Kral Q., Sinclair C. A., 2020, MNRAS, 491, 782
Yi S., Demarque P., Kim Y.-C., Lee Y.-W., Ree C. H., Lejeune T., Barnes S., 2001, ApJS, 136, 417
Yu X. et al., 2021, Nat. Astron., 5, 822
Zechmeister M., Kürster M., 2009, A&A, 496, 577
Zeng L. et al., 2019, Proc. Natl. Acad. Sci., 116, 9723
Zink J. K. et al., 2021, AJ, 162, 259

APPENDIX A: SPECTROSCOPIC DATA

Table A1 contains the log of the CHEOPS observations of K2-370. The file key (first column) is a unique identifier that can be used to retrieve the data from the CHEOPS archive. Tables A2 and A3 contain the time-series of the RV data and spectroscopic activity indicators (FWHM, BIS, *S*-index), along with their uncertainties, obtained from the HARPS-N and HARPS spectra, respectively

Downloaded from https://academic.oup.com/mnras/article/535/1/531/7819156 by Uni PD user on 04 September 2025

Table A1. CHEOPS observing times and file keys.

File key	UTC start	UTC end	Visit duration (s)
CH_PR220007_TG000701_V0300	2021-11-09T18:48:09	2021-11-10T01:16:20	23 291
CH_PR220007_TG000702_V0300	2022-01-02T08:11:28	2022-01-02T13:59:38	20 890

Table A2. HARPS-N RVs and activity diagnostics.

Time (BJD−2 450 000)	RV ($m\,s^{-1}$)	σ_{RV} ($m\,s^{-1}$)	CCF FWHM ($m\,s^{-1}$)	σ_{FWHM} ($m\,s^{-1}$)	CCF BIS ($m\,s^{-1}$)	σ_{BIS} ($m\,s^{-1}$)	S_{MW} (dex)	$\sigma_{S_{MW}}$ (dex)
58086.553143	−22 159.12	6.18	8028.25	12.35	13.56	12.35	0.2969	0.0040
58088.586873	−22 124.03	2.33	8042.78	4.67	−19.89	4.67	0.3173	0.0010
58098.455554	−22 137.73	2.76	8108.58	5.51	-7.00	5.51	0.3325	0.0014
58102.504522	−22 109.14	4.27	8048.16	8.53	−26.22	8.53	0.3204	0.0025
58102.646627	−22 113.30	2.73	8050.98	5.47	−29.15	5.47	0.3347	0.0014
58103.513635	−22 100.47	3.64	8086.73	7.28	−30.21	7.28	0.3126	0.0021
58111.586232	−22 147.58	5.69	8100.13	11.39	10.89	11.39	0.3114	0.0037
58112.400620	−22 138.33	3.10	8066.16	6.19	-2.85	6.19	0.3262	0.0017
58117.424682	−22 089.58	6.72	8092.91	13.44	−27.86	13.44	0.3207	0.0042
58117.489059	−22 090.88	5.16	8068.33	10.31	−48.21	10.31	0.3219	0.0030
58119.437064	−22 089.62	9.52	8110.54	19.04	−48.67	19.04	0.3227	0.0069
58120.482620	−22 079.77	7.63	8203.17	15.27	−32.18	15.27	0.3407	0.0051
58132.364217	−22 083.54	2.15	8124.38	4.30	−30.62	4.30	0.3413	0.0010
58410.675542	−22 136.43	5.54	8060.87	11.08	-3.35	11.08	0.3336	0.0033
58415.769808	−22 139.11	2.05	8032.16	4.09	−14.27	4.09	0.3348	0.0008
58448.631942	−22 077.27	2.14	8134.18	4.28	−35.96	4.28	0.3547	0.0009
58451.497063	−22 166.16	3.73	8059.49	7.46	23.90	7.46	0.3312	0.0020
58451.652945	−22 172.84	2.73	8041.07	5.45	18.41	5.45	0.3213	0.0013
58454.487594	−22 124.17	2.32	8082.20	4.65	−12.97	4.65	0.3236	0.0010
58454.610317	−22 132.11	2.75	8079.40	5.49	-9.98	5.49	0.3160	0.0014
58456.449396	−22 134.78	2.69	8019.03	5.38	−22.75	5.38	0.3210	0.0013
58477.563016	−22 140.33	6.17	8162.66	12.34	1.52	12.34	0.3088	0.0039
58478.589182	−22 157.87	2.58	8078.10	5.15	12.26	5.15	0.3282	0.0012
58478.635063	−22 160.91	2.72	8063.66	5.44	25.77	5.44	0.3248	0.0014
58479.516601	−22 138.54	1.98	8039.98	3.96	−16.72	3.96	0.3273	0.0008
58479.619127	−22 136.81	2.00	8034.01	4.00	−13.25	4.00	0.3345	0.0009
58480.537187	−22 104.12	2.13	8065.06	4.26	−47.45	4.26	0.3247	0.0009
58481.497158	−22 113.11	3.83	8115.81	7.65	-9.26	7.65	0.3191	0.0021
58481.598727	−22 127.06	3.66	8123.12	7.33	−12.17	7.33	0.3195	0.0020
58482.452905	−22 152.56	2.51	8097.58	5.03	14.29	5.03	0.3137	0.0011
58482.596087	−22 153.53	1.93	8073.25	3.86	6.63	3.86	0.3253	0.0008
58483.459313	−22 146.78	2.35	8028.90	4.71	-2.48	4.71	0.3206	0.0010
58483.598639	−22 147.30	2.60	8037.55	5.20	−11.08	5.20	0.3198	0.0012
58484.433571	−22 136.93	3.29	8017.90	6.58	−27.81	6.58	0.3096	0.0017
58484.585011	−22 131.65	2.71	8016.93	5.42	−29.96	5.42	0.3141	0.0013
58487.494835	−22 100.30	2.81	8091.02	5.61	−22.28	5.61	0.3433	0.0014
58487.593974	−22 102.28	2.72	8094.15	5.43	−30.70	5.43	0.3415	0.0014
58488.471490	−22 107.56	2.38	8105.01	4.75	−21.81	4.75	0.3441	0.0011
58488.602331	−22 099.57	2.95	8122.51	5.90	−35.88	5.90	0.3528	0.0016
58489.520344	−22 093.98	2.04	8146.63	4.08	−22.15	4.08	0.3589	0.0009
58489.604444	−22 094.38	3.02	8152.61	6.04	−15.11	6.04	0.3527	0.0016
58502.450558	−22 093.26	2.86	8116.14	5.71	−30.55	5.71	0.3550	0.0014
58502.580533	−22 083.19	5.00	8096.58	9.99	−20.77	9.99	0.3677	0.0032
58503.402222	−22 101.28	3.00	8124.03	6.00	−15.64	6.00	0.3567	0.0015
58503.527306	−22 095.33	1.93	8134.02	3.85	−14.01	3.85	0.3592	0.0008
58504.496118	−22 117.87	2.84	8151.02	5.68	11.75	5.68	0.3478	0.0014

Downloaded from https://academic.oup.com/mnras/article/535/1/531/7819156 by Uni PD user on 04 September 2025

Table A2 – *continued*

Time (BJD−2 450 000)	RV ($m\,s^{-1}$)	σ_{RV} ($m\,s^{-1}$)	CCF FWHM ($m\,s^{-1}$)	σ_{FWHM} ($m\,s^{-1}$)	CCF BIS ($m\,s^{-1}$)	σ_{BIS} ($m\,s^{-1}$)	S_{MW} (dex)	$\sigma_{S_{MW}}$ (dex)
58505.442190	−22 154.81	2.71	8087.56	5.41	25.30	5.41	0.3389	0.0013
58518.431463	−22 136.93	5.19	8125.69	10.37	18.89	10.37	0.3491	0.0032
58519.376304	−22 133.69	10.93	8108.78	21.87	39.49	21.87	0.3075	0.0079
58520.377284	−22 126.75	2.82	8040.40	5.65	−30.02	5.65	0.3348	0.0014
58520.478461	−22 121.76	2.98	8059.08	5.96	−25.73	5.96	0.3317	0.0016
58521.377939	−22 099.94	4.77	8069.77	9.53	−37.33	9.53	0.3417	0.0029
58521.511799	−22 099.12	3.36	8092.41	6.72	−40.63	6.72	0.3316	0.0019
58522.415437	−22 118.34	2.38	8106.08	4.76	0.24	4.76	0.3254	0.0011
58523.406830	−22 124.68	1.88	8091.19	3.75	-8.25	3.75	0.3364	0.0007
58523.555456	−22 125.92	3.10	8090.02	6.21	-7.51	6.21	0.3349	0.0019
58524.383440	−22 120.85	2.18	8086.52	4.36	-7.38	4.36	0.3337	0.0009
58525.383065	−22 113.12	3.07	8073.33	6.13	−19.71	6.13	0.3405	0.0016
58526.364552	−22 104.76	1.98	8104.53	3.96	−18.96	3.96	0.3453	0.0008
58527.408566	−22 125.98	2.39	8109.90	4.77	−18.03	4.77	0.3294	0.0011
58527.495391	−22 128.58	2.96	8104.83	5.92	-4.92	5.92	0.3410	0.0015
58528.378223	−22 116.33	3.25	8090.09	6.50	-3.75	6.50	0.3385	0.0016
58536.434630	−22 117.51	5.73	8069.21	11.46	−16.35	11.46	0.3518	0.0037
58537.452789	−22 116.30	7.18	8059.34	14.35	−25.98	14.35	0.3039	0.0052
58538.451386	−22 114.05	3.45	8078.23	6.89	−33.65	6.89	0.3285	0.0020
58539.460541	−22 120.20	2.83	8089.33	5.65	−21.50	5.65	0.3270	0.0015
58544.346306	−22 095.78	2.03	8139.19	4.06	−31.91	4.06	0.3456	0.0008
58545.345560	−22 119.28	2.10	8155.93	4.20	0.35	4.20	0.3492	0.0009
58546.345096	−22 139.21	5.41	8100.63	10.81	19.09	10.81	0.3524	0.0034
58547.386937	−22 115.11	2.74	8082.47	5.48	−16.57	5.48	0.3520	0.0014
58559.407706	−22 141.94	2.53	8152.35	5.07	6.18	5.07	0.3333	0.0013
58561.368853	−22 130.19	2.83	8066.32	5.66	-9.50	5.66	0.3383	0.0015
58562.365903	−22 111.24	3.91	8064.25	7.81	-8.61	7.81	0.3293	0.0023
58563.365220	−22 131.22	3.15	8098.56	6.30	−11.06	6.30	0.3326	0.0017
58565.363691	−22 116.36	3.21	8067.74	6.42	−27.46	6.42	0.3231	0.0018
58566.361956	−22 102.84	1.95	8083.18	3.90	−18.15	3.90	0.3307	0.0008

Downloaded from https://academic.oup.com/mnras/article/535/1/531/7819156 by Uni PD user on 04 September 2025

Table A3. HARPS RVs and activity diagnostics.

Time (BJD−2 450 000)	RV ($m\,s^{-1}$)	σ_{RV} ($m\,s^{-1}$)	CCF FWHM ($m\,s^{-1}$)	σ_{FWHM} ($m\,s^{-1}$)	CCF BIS ($m\,s^{-1}$)	σ_{BIS} ($m\,s^{-1}$)	S_{MW} (dex)	$\sigma_{S_{MW}}$ (dex)
59854.774758	−21 976.27	3.00	7967.50	11.27	18.50	4.24	0.3032	0.0083
59854.862404	−21 979.19	3.50	7952.27	11.25	25.18	4.95	0.2836	0.0111
59855.779565	−21 989.89	3.13	7930.29	11.22	37.58	4.43	0.2934	0.0091
59855.868057	−21 992.31	2.68	7937.58	11.23	20.77	3.80	0.2948	0.0076
59856.777126	−22 006.66	4.46	7929.86	11.21	15.77	6.31	0.2334	0.0149
59856.866879	−22 006.79	4.16	7908.30	11.18	25.54	5.89	0.2776	0.0144
59858.862623	−22 014.63	5.21	7895.65	11.17	-2.89	7.36	0.2346	0.0192
59859.768310	−21 980.80	2.93	7875.11	11.14	−10.00	4.14	0.2635	0.0084
59859.859671	−21 984.90	2.96	7857.86	11.11	−11.49	4.19	0.2712	0.0088
59860.752278	−21 986.03	3.26	7896.10	11.17	−17.60	4.61	0.2768	0.0096
59860.867657	−21 983.77	3.94	7897.83	11.17	−20.18	5.57	0.2749	0.0130
59881.736143	−21 958.75	2.55	7994.49	11.31	12.72	3.60	0.3271	0.0070
59881.810846	−21 961.31	2.81	7996.87	11.31	9.33	3.97	0.3080	0.0087
59882.718557	−21 979.91	2.86	7991.41	11.30	22.27	4.04	0.3177	0.0080
59882.833922212	−21 985.92	2.74	7983.11	11.29	32.76	3.88	0.3089	0.0089
59883.720796	−21 996.66	4.12	7965.49	11.26	35.44	5.83	0.2903	0.0128
59883.785985	−22 000.43	5.76	7950.12	11.24	12.25	8.15	0.3094	0.0197
59884.710025	−22 002.60	4.32	7931.32	11.22	40.92	6.11	0.2936	0.0137
59884.760583	−22 005.97	3.78	7936.65	11.22	19.99	5.34	0.2883	0.0115
59885.707377	−21 989.22	2.76	7912.19	11.19	15.86	3.90	0.2940	0.0077
59885.795575	−21 989.29	3.37	7924.79	11.21	3.95	4.76	0.2858	0.0107
59886.731430	−21 986.12	2.77	7902.23	11.18	23.08	3.91	0.3001	0.0077
59886.829363	−21 985.50	2.61	7920.05	11.20	7.68	3.69	0.3028	0.0086
59897.680505	−21 995.10	3.36	7956.10	11.25	17.17	4.75	0.3011	0.0100
59897.777996	−21 993.81	2.91	7958.18	11.25	23.67	4.11	0.3186	0.0093
59898.682594	−21 991.72	3.27	7946.17	11.24	29.74	4.63	0.3141	0.0095
59898.799819	−21 996.80	3.97	7939.79	11.23	19.49	5.61	0.3102	0.0135
59899.683847	−21 988.20	2.90	7946.64	11.24	12.67	4.10	0.3204	0.0083
59899.780088	−21 985.84	2.98	7924.23	11.21	24.95	4.220 22	0.2986	0.0092
59900.680701	−21 981.10	3.05	7954.40	11.25	20.37	4.32	0.3298	0.0089
59900.758712	−21 986.14	3.42	7934.49	11.22	24.91	4.83	0.2909	0.0109
59901.680192	−22007.11	3.66	7928.62	11.21	37.89	5.18	0.3187	0.0108
59941.596924	−21 975.82	2.95	7928.16	11.21	19.80	4.17	0.2972	0.0098
59941.682012	−21 986.89	4.00	7919.92	11.20	-6.06	5.65	0.2745	0.0155
59942.568962	−21 978.96	4.02	7915.43	11.19	26.51	5.68	0.2662	0.0141
59942.685403	−21 994.24	3.31	7909.88	11.19	15.70	4.68	0.2836	0.0130
59943.570233	−21 997.66	2.85	7916.11	11.20	46.94	4.04	0.2923	0.0093
59943.657058	−22 002.82	2.84	7907.14	11.18	19.32	4.01	0.2920	0.0105
59944.640585	−22 003.06	5.83	7863.51	11.12	25.49	8.25	0.2591	0.0243
59951.582953	−21 930.08	3.48	7990.78	11.30	21.99	4.92	0.3053	0.0124
59951.645241	−21 921.10	4.35	8015.51	11.34	43.34	6.16	0.2913	0.0166
59952.575323	−21 971.39	3.88	7926.43	11.21	26.01	5.48	0.3271	0.0139
59952.644011	−21 968.70	4.47	7974.17	11.28	44.27	6.33	0.3097	0.0172
59953.581903	−21 977.86	2.79	7920.23	11.20	22.66	3.95	0.3097	0.0096
59953.650475	−21 978.51	2.97	7935.89	11.22	10.29	4.20	0.3220	0.0107
59954.570821	−21 987.19	3.27	7897.04	11.17	8.25	4.62	0.3488	0.0113
59954.640331	−21 983.20	3.21	7925.61	11.21	21.02	4.54	0.3286	0.0125
59955.625636	−21 974.28	2.85	7920.92	11.20	11.14	4.03	0.3234	0.0099
59955.669140	−21 972.23	2.58	7906.86	11.18	5.51	3.65	0.3306	0.0089
59956.552530	−21 979.16	2.75	7903.54	11.18	16.79	3.89	0.3267	0.0088
59956.685704	−21 984.50	3.09	7908.63	11.18	17.88	4.37	0.3489	0.0112
59957.594057	−22 004.87	4.72	7893.45	11.16	32.28	6.67	0.3336	0.0184
59958.546942	−22 006.36	3.72	7880.54	11.14	17.67	5.26	0.2917	0.0134

Downloaded from https://academic.oup.com/mnras/article/535/1/531/7819156 by Uni PD user on 04 September 2025

Table A3 – *continued*

Time (BJD−2 450 000)	RV ($m\,s^{-1}$)	σ_{RV} ($m\,s^{-1}$)	CCF FWHM ($m\,s^{-1}$)	σ_{FWHM} ($m\,s^{-1}$)	CCF BIS ($m\,s^{-1}$)	σ_{BIS} ($m\,s^{-1}$)	S_{MW} (dex)	$\sigma_{S_{MW}}$ (dex)
59958.661089	−22 004.09	3.09	7882.22	11.15	8.82	4.38	0.3113	0.0119
59959.609101	−22 013.20	2.97	7847.09	11.10	18.54	4.19	0.2951	0.0105
59960.548015	−21 999.12	3.46	7863.41	11.12	–5.96	4.89	0.3283	0.0127
59960.635832	−21 995.17	2.81	7865.31	11.12	-9.58	3.98	0.3169	0.0102
59972.548081	−22 018.87	3.01	7881.78	11.15	20.18	4.25	0.2859	0.0092
59972.597961	−22 018.49	3.12	7872.77	11.13	38.45	4.41	0.2893	0.0105

This paper has been typeset from a TEX/LATEX file prepared by the author.

Downloaded from https://academic.oup.com/mnras/article/535/1/531/7819156 by Uni PD user on 04 September 2025

© 2024 The Author(s).
Published by Oxford University Press on behalf of Royal Astronomical Society. This is an Open Access article distributed under the terms of the Creative Commons Attribution License (https://creativecommons.org/licenses/by/4.0/), which permits unrestricted reuse, distribution, and reproduction in any medium, provided the original work is properly cited.